Orbital control on the thermocline structure during the past 568 kyr in the Solomon Sea, southwest equatorial pacific

Lo Li [1, 2, 3, *], Shen Chuan-Chou [1, 3, 4], Zeeden Christian [5], Tsai Yi-Hsueh [1, 2], Yin Qiuzhen [6], Yang Chun-Chih [1, 2, 3], Chang Tzu-Ling [7], Su Yu-Chu [7], Mii Horng-Sheng [8], Chuang Chih-Kai [1, 2, 3], Chem Yi-Chi [1]

[1] Department of Geosciences, National Taiwan University, Taipei, Taiwan
[2] Paleoceanography Laboratory, National Taiwan University, Taipei, Taiwan
[3] Research Center for Future Earth, National Taiwan University, Taipei, Taiwan
[4] High Precision Mass Spectrometry and Environment Change Laboratory (HISPEC), National Taiwan University, Taipei, Taiwan
[5] LIAG-Leibniz Institute for Applied Geophysics, Geozentrum Hannover, Hannover, Germany
[6] Georges Lemaitre Center for Earth and Climate Research, Earth and Life Institute, Université Catholique de Louvain, Louvain-la-Neuve, Belgium
[7] Taipei First Girls High School, Taipei, Taiwan
[8] Department of Earth Sciences, National Taiwan Normal University, Taipei, Taiwan

* Corresponding author : Li Lo, email address : lilo115@ntu.edu.tw

Abstract :

The Solomon Sea is the main source of the equatorial undercurrent and the main crossroad of the equatorial region and the South Pacific Ocean. Based on multi-species planktonic foraminiferal geochemical proxies, here we reconstruct the vertical thermal-hydrological variabilities over the last 568,000 years in the Solomon Sea. The proxies used include the differences between δ18O data of the surface dweller Globigerinoides ruber (white) and the subsurface dweller Pulleniatina obliquiloculata (Δδ18Oc), the sea surface temperature (SST) and the upper thermocline temperature (UTT) as well as their differences (ΔT), and the seawater oxygen isotope differences (Δδ18Ow). Both the SST and UTT records feature similar timing of warming, which is 2–4 kyr earlier than the G/IG boundaries for the past six terminations. Different from the other five terminations, both SST and UTT records of Termination V show a persistent and early increase of 5–7 °C in 10 kyr since ~440 ka. On the obliquity band, higher SST and UTT correspond to larger obliquity, suggesting higher subtropical South Pacific input. This argument is supported by lower ΔT and higher Δδ18Ow. In the meantime, higher SST and UTT also correspond to precession minimum, suggesting an expansion of the mixed layer with lower ΔT and greater Δδ18Ow. Our results show complex interactions between precipitation-evaporation and water masses exchange in the Solomon Sea. The clear obliquity signal observed in multiple proxies reveals strong interactions between the Solomon Sea and the mid-high latitude South Pacific regions.

Highlights

► High resolution surface and subsurface reconstructions in the south marginal warm pool region during the past 568,000 years ► Strong precession and obliquity pacings suggest complex atmospheric and oceanic processes in the Solomon Sea. ► Termination V in Solomon Sea shows very early and persistent warming, induced by both insolation and CO_2 forcings.

Keywords : Thermocline structure, Orbital forcing, Western pacific warm pool, Terminations

1. Introduction

The Western Pacific Warm Pool (WPWP) is the major contributor of latent heat and moisture to Earth's climate systems. Strong vertical convection to the troposphere is induced by an annual sea surface temperature (SST) higher than 28°C in the region (Cane, 1988; Ganachaud et al., 2014). Large atmospheric circulation systems in both the zonal (Walker Circulation) and meridional (Hadley Circulation) directions are crucial to regional and global energy and ocean circulation systems. For the hydrological impact of WPWP, the trade winds and the position of the Intertropical Convergence Zone (ITCZ), which are tightly related to the WPWP extent and variations (Dang et al., 2012; Tachikawa et al., 2012), are crucial for the precipitation in both hemispheres. Modern observations have revealed the impact of the WPWP variability on seasonal-to-decadal timescales. Most importantly, the El Niño-Southern Oscillation (ENSO) varies at 2-7 years pacing. A weakened trade wind system accompanied by a warming in the central-eastern equatorial Pacific has profound effects on global precipitation and surface temperature changes (Germineaud et al., 2016; Grenier et al., 2011; Grenier et al., 2014).

Besides surface convection and circulation, the subsurface ocean circulation also plays a crucial role for the WPWP variability. Thermocline circulation links not only subsurface water to the atmosphere in the upwelling region, but also the middle latitude subtropical gyre and even sub-polar regions to the equatorial region (Gasparin et al., 2012; Germineaud et al., 2016; Grenier et al., 2011). The thermocline in the western equatorial Pacific can be deepened to 100-200 m due to the wind-transported surface waters and the narrowed passages between the Indian and Pacific Oceans. In contrast, shallow thermocline of 25-50 m occurs in the eastern Pacific region due to the strong upwelling and surface divergence. Due to the tight link between the surface water

dynamics and the subsurface thermocline circulation in the equatorial Pacific Ocean, the understanding of the vertical thermal-hydrological variations is crucial for understanding the mechanisms of the WPWP variabilities on different timescales.

In order to understand the past warm pool dynamics in the geological past, numerous reconstructions of the warm pool thermal and hydrological histories have been conducted. Several SST records have been used to calculate the zonal temperature gradient evolution since the past 5 million years to reconstruct the surface thermal gradient and the potential zonal thermocline structure variations (Lea et al. 2000; de Garidel-Thoron et al., 2005; Wara et al., 2005). However, these studies are not specific to vertical water column temperature-salinity changes. Subsurface planktonic foraminifera records have been reconstructed to fill the apparent knowledge gap. Pena et al. (2008) demonstrated the power of using both surface and subsurface temperature (Mg/Ca inferred seawater temperatures) and hydrological proxies (ice volume corrected seawater oxygen isotopes, $\delta^{18}O_{w\text{-}ivc}$) to assess the millennial time scales variabilities during the past ~280 kyr. Xu et al. (2008; 2010) applied a similar method mainly in the western Pacific and eastern Indian Ocean to reconstruct the vertical water structure of the Indonesian Throughflow (ITF), and the interactions between these regions. Further studies implied the importance of the subsurface water structure in the WPWP regions for reconstructing the specific subsurface mixing (Boillet et al., 2011), understanding regional monsoonal induced upwelling variabilities, calculating the ocean heat content from vertical profiles (Dang et al., 2012, Dang et al., 2020; Ford et al., 2018; Nascimento et al., 2021; Pang et al., 2021, Rustic et al., 2020; Wang et al., 2018; Weiss et al., 2021; Zhang et al., 2021), and building interhemispheric mixing history of intermediate/mode waters (Jian et al., 2021). However, these high temporal resolution studies show complicate patterns from region to region. Furthermore, the

shorter time duration limits our understanding of certain warmer-than-present periods, e.g. MIS 5e, 9, and 11c, and of the effects of different astronomical parameters, e.g. precession (Jian et al., 2020; Zhang et al., 2020) and/or obliquity (Hollstein et al., 2018: Hollstein et al., 2020) cycles.

Previous studies focused mainly on the core region. The southwestern part of the WPWP, which links the South surface and subsurface waters from the south Pacific gyre through the South Equatorial Current (SEC) in the Coral and Solomon Seas, receives less attention. The warm and salty subsurface waters from the south Pacific gyre penetrate seasonally across the Papua New Guinea (PNG) region, compensate and become one of the main sources of the Equatorial Under Current (EUC) (**Figure 1**, Cravatte et al., 2009; Cravatte et al., 2011, Ganachaud et al., 2014; Ganachaud et al., 2017; Gasparin et al., 2012; Germineaud et al., 2016; Germineaud et al., 2021; Grenier et al., 2011, Grenier et al., 2014).

Despite the important role of the southwestern warm pool region in ocean circulation, climate, and nutrient of regional to global system, there were rather few paleoceanographic studies. Lo et al. (2014a) firstly demonstrated the millennial-scale SST and surface $\delta^{18}O_w$ variabilities during the last termination. The meridional SST contrast between the northern and southern WPWP supports the southward movement of the Hadley Circulation and ITCZ during past sudden cooling events in the northern hemisphere (Heinrich event 1 and Younger Dryas). This finding suggests that the equatorial Pacific is sensitive to the high-latitude related climate changes and could play an important role in transporting climatic signals through both thermal and hydrological changes. Further study shows that the atmospheric pressure gradient between the Siberian high and the Australian low induced by orbital forcing would

affect the meridional equatorial precipitation belt (Liu et al., 2015). Lo et al. (2017) calculated the climatic sensitivity between SST and greenhouse gases radiation forcing and revealed the heterogeneity across the equatorial Pacific Ocean. However, there is still a knowledge gap on how the glacial/interglacial (G/IG) boundary condition changes impact the vertical water column and the thermal and hydrological histories in the Solomon Sea region.

In this study, we reconstruct the vertical thermal-hydrological-nutrient gradients in the Solomon Sea during the past 568 kyr. By using *Globigerinodies ruber* and *Pulleniatina obliquiloculata* planktonic multiple geochemical proxies (Mg/Ca elemental ratios and $\delta^{18}O$ of carbonate test, $\delta^{18}O_c$) and ice volume corrected seawater oxygen isotope ($\delta^{18}O_{w-ivc}$), we assess the main phase relationship between orbital forcing and specific climatic parameters across the G/IG cycles.

2. Regional setting

The Solomon Sea is a semi-closed basin located in the southwest equatorial Pacific Ocean. Surrounded by PNG, the Solomon Islands, and the New Britain Islands, straits and channels control the main water exchange. For example, the Solomon Strait controls the exchange of water masses between equatorial Pacific Ocean and Solomon Sea, and is the main pathway for the SEC traveling northward across the PNG and to join in the ITF. The seasonal reversal of the Indonesian-Australia monsoon system brings moisture from surrounding seas as strong precipitation in the high mountain regions of PNG. The monsoon wind also controls the current direction (**Figure 1**).

The SEC enters the Solomon Sea mainly through the Coral Sea (**Figure 1**). Vertical mixing through meso-scale eddy dynamics is the most important process to

mix signals of different sources of water masses. The main sources of the EUC are originally from the mode- and intermediate waters from both the Northern and Southern hemispheric subtropical-sub-polar regions (Qu et al., 2013) and then flow from coastal PNG to the eastern equatorial Pacific. Therefore, the high-low latitude oceanic connections through this circulation pathway eventually upwelled in the eastern equatorial regions, such as the EEP region. The nutrient-enriched subsurface waters are transported by the ocean from the high latitudes and also modified by the regional supply from specific regions. For example, considerable input of trace elements from the Solomon Sea was observed due to the strong mixing and intense weathering from high mountain regions and extremely high precipitation in and around the PNG region (Ganachaud et al., 2017).

Systematic observations suggest the Solomon Sea being the main pathway between the South to equatorial Pacific even to the Indian Ocean through the ITF (Gasparin et al., 2012). On inter-annual timescale, the ENSO is a main driver. During the ENSO phase, the surface and subsurface systems in the Solomon Sea are mainly driven by the fresher and cooler equatorial Pacific Ocean (Ganachaud et al., 2017). Due to the heavy precipitation in the PNG region (> 5000 mm/yr), large amounts of major nutrients and rare earth elements are transported to the Solomon Sea and become the major regional and even global contributor (Ganachaud et al., 2017). Through the high-to low-latitude oceanic tunneling and regional weathering input, the Solomon Sea is also the main contributor of elements of Al and Mn to the world's oceans. The nutrients originally from the mid-high latitude water masses also re-surface around 150°E and contribute to the EUC system, and eventually well up in the EEP region (Qu et al., 2013).

The role of Solomon Sea in water mixing and transportation of nutrients and rare elements is therefore crucial, and the Solomon Sea SST may be an important factor for atmospheric-oceanic dynamics and precipitation belt changes during terminations (Lo et al., 2014a, 2017; Liu et al., 2015).

3. Material and methods

3.2 Site MD05-2925

A marine sediment core, 28.38 m in length, was obtained at site MD05-2925 (9.3°S, 151°E, water depth 1667 m) during the 2005 Past Equatorial Climate: Tracking El Niño (PECTEN) cruise, which was supported by the International Marine and Climate Changes (IMAGES) Project, through the research vessel Marion Dufresne. This site is located on the Woodlark rise, Solomon Sea. The annual average SST is 28.5 °C and the seasonal variation ranges from 27.4 to 29.4 °C (Schlitzer, 2021; **Figure 1**).

3.3 Age model

The MD05-2925 age model was established using accelerator mass spectrometry radiocarbon (AMS ^{14}C) dates and benthic foraminiferal oxygen isotope stratigraphic correlation. In this study, we summarized and revised the entire core back to 568 kyr from previous studies (Lo et al., 2014a; Lo et al., 2017; Lo et al., 2021). All benthic foraminiferal tests were >250 μm in size, and 2–5 tests of multi species benthic foraminiferal (*Uvigerina* spp., *Bulimina* spp., *Planulina wuellerstorfi*, and *Pyrgo* spp.) were used for $\delta^{18}O$ measurement. The compiled benthic foraminiferal $\delta^{18}O$ data were correlated to the global benthic foraminiferal $\delta^{18}O$ stack (LR04, Lisiecki and Raymo, 2005) (**Supplementary figure 1a**). Three main Milankovitch cycles are filtered and carefully examined between MD05-2925 benthic oxygen isotope stratigraphy and

LR04. All peaks are correlated to each other well (<5%) in each cycle (**Supplementary figure 1b-d**).

3.4 Planktonic foraminifera

Globigerinoides ruber (white) is a spinose species that dwell in the mixed layer and upper thermocline from 0–25 m (Lakhani et al., 2022). *Pulleniatina obliquiloculata* is expected to mainly dwell in the seasonal thermocline (e.g., Lakhani et al., 2022). Plankton tow studies showed that the living *P. obliquiloculata* dwells from the sea-surface to the deep thermocline, but usually concentrate from 50-150-m water depth (**Figure 1e**, Dang et al., 2018; Lakhani et al., 2022).

3.5 Stable C-O isotope analyses

In total, 40–60 planktonic foraminifera *G. ruber* (white, *s.s.*, 250–300 μm) were picked for carbon/oxygen isotopic and Mg/Ca determinations. For each of the paired isotope-Mg/Ca measurements, 20–30 tests were gently crashed and mixed. For the isotope measurements, the samples were ultrasonicated 3–4 times, immersed in NaOCl for 24-hr, and dried. The cleaned samples were measured on a Micromass IsoPrime isotope ratio mass spectrometer (IRMS) at the National Taiwan Normal University. Analytical reproducibility is ±0.05‰ (1σ, N = 701) with respect to the Vienna Pee Dee Belemnite (VPDB, Lo et al., 2013).

3.6 Mg/Ca analysis and seawater oxygen isotope calculations

For Mg/Ca measurements, the crushed shells were placed in Teflon vials. The cleaning procedure followed that of Lo et al. (2014b). Cleaned samples were dissolved in 5% HNO_3 and measured using a Thermo-Finnigan Element II sector field inductively coupled plasma mass spectrometer (SF-ICP-MS) at the High-Precision Mass

Spectrometry and Environment Change Laboratory (HISPEC), Department of Geosciences, National Taiwan University. The external uncertainty is ±0.32% (2-RSD). Dissolution effects in the MD05-2925 core have been addressed by Lo et al. (2017). We also measured average *G. ruber* shell weight for the interval from 568-361 ka. The mean signal test weight is similar to previous reports (**Supplementary figure 2c**).

We adopted Anand et al. (2003) composite Mg/Ca-temperature equation for both specie due to the wider range of temperature reconstruction especially on the G/IG cycles. $\delta^{18}O$ value in planktonic foraminifera includes variabilities of temperature, salinity, water mass and sea level effects. We followed previous study (Lea et al., 2000) and used cultured *Orbulina universa* low light equation to calculate for both species $\delta^{18}O_w$ (Bemis et al., 1998). Sea level reconstruction by Spratt and Lisiecki (2016) was used to calculate ice volume corrected sea water oxygen isotope ($\delta^{18}O_{w\text{-ivc}}$) for both species. We also compared $\delta^{18}O_{w\text{-ivc}}$ derived from different sea level reconstructions (**Supplementary figure 3a-b**).

3.7 Solomon Sea vertical thermal and hydrological profile reconstruction

In order to reconstruct the vertical stratification between surface and upper thermocline in the Solomon Sea, we calculated the differences between *G. ruber* and *P. obliquiloculata* geochemical proxy data ($\delta^{18}O_c$, Mg/Ca derived temperature, and $\delta^{18}O_w$). To avoid the time resolution differences among two species and three geochemical proxies, we smoothed all geochemical records to 1-kyr time resolution by using Analyseries software (Paillard et al., 1996), and calculated differences between two planktonic foraminifera. $\Delta\delta^{18}O_c$, ΔT, and $\Delta\delta^{18}O_w$ records are discussed in section 5.

3.8 Timeseries analyses

All MD05-2925 data for single spectrum was firstly resampled to 1-kyr resolution and analyzed by the REDFIT software (Schulz and Mudelsee, 2002). Insolation and orbital parameters generated by Analyseries software are in 1-kyr step as well, based on the La2004 solution (Laskar et al., 2004). Cross spectral analysis was done using ARAND (Howell et al., 2006).

Orbital cycles (eccentricity, obliquity, and precession) are filtered by Gaussian filtering using Analyseries cut-off frequencies of 0.0125-0.077 and 0.027-0.023, and 0.054-0.041, respectively (Paillard et al., 1996). Note that both the limited length of the time series and possibly changing phases throughout this interval limit precise phase statements. We reported our results in two ways. One is to average only the results that have high coherency >0.6 (80% confidence; columns that labeled in gray, **Table 1**) and another way is to average all data in certain periodicity. The numbers in white columns are the coherency that less than 0.6. We found no significant difference for most of the results.

4. Results

4.1 Age model

The composite benthic foraminiferal oxygen isotope stratigraphy with single species planktonic foraminiferal AMS ^{14}C age model of MD05-2925 during 0-462 kyr was reported in previous studies (Lo et al., 2017; Lo et al., 2021). Here we applied the same chronological method through the whole core. With the tuning to a global composite benthic foraminiferal oxygen isotope stratigraphy (LR04; Lisiecki and Raymo, 2005), an age of 568 kyr was determined for the bottom of MD05-2925 core.

The range of the sedimentation rate during the interval of 568 kyr to 462 kyr is 5-10 cm/kyr which is similar to the previously reported rate (**Supplementary figure 1**).

4.2 Planktonic foraminifera oxygen isotopes

The oxygen isotope ratios of both planktonic foraminifera species show strong glacial-interglacial variability, ranging from -2.8 to -0.8‰ and -1.7 to 0.8‰ for *G. ruber* and *P. obliquiloculata*, respectively (**Figure 2a, b**). "Saw-tooth" type rapid terminations and gradually increasing values during glacial inceptions are a clear and common pattern. Exceptionally positive values during glacial periods are particularly apparent in MIS 6, but MIS 14 is characterized by relatively higher $\delta^{18}O$ values compares with other glacial periods which indicates a mild glacial. Peak glacial $\delta^{18}O$ values of -1.1 and 0.4‰ are similar for MIS 2, 10, and 12 in both surface and subsurface water dwellers. During interglacial periods, *G. ruber* shows slightly higher values for MIS 7, 13 and 15 compared to peak interglacial periods of e.g., mid-Holocene, MIS 5e, 9e, 11c. However, *P. obliquiloculata* shows similar $\delta^{18}O$ values of -1.5‰ during the interglacial periods.

4.3 Mg/Ca ratios and inferred seawater temperatures

The Mg/Ca ratios and inferred temperature data derived from *G. ruber* and *P. obliquiloculata* vary from 3.5-6.0 and 2.0-4.0 mmol/mol (**Supplementary figure 2a, b**) and 24-30 ºC and 20-26 ºC (**Figure 2c, d**), respectively. Glacial-interglacial amplitudes range from 3-4 ºC in the mixed layer up to 5 ºC in the subsurface water. Overall analytical and Mg/Ca-temperature calibration errors are considered followed Mohtadi et al. (2014) method. The averaged SST and UTT errors are ±0.7 and ±0.9 ºC, respectively (**Figure 2**).

Relative cool interglacial periods are observed during MIS 7, 13 and 15 comparing to other warming periods, such as mid-Holocene, MIS 5e, 9e, and 11c, in the mixed layer. Subsurface UTT record shows similar peak temperature of 2 6°C (**Figure 2d**). Seawater temperature values at MIS 5a and 5c are ~28 and 23 °C for surface and subsurface waters, which are ~2 and 3 °C lower than at MIS 5e. Glacial maxima show constant and similar temperature of 24 °C for the surface and 21 °C for the subsurface layers.

4.4 $\delta^{18}O_w$ and ice volume corrections

The derived $\delta^{18}O_w$ records express clear G/IG cycles for both species and ranges from -0.5 to 1.5‰ and -0.5 to 2.0‰ for *G. ruber* and *P. obliquiloculata*, respectively (**Supplementary figure 2d, e**). Overall surface and subsurface $\delta^{18}O_w$ errors are 0.18‰ and 0.21‰, respectively (Mohtadi et al., 2014).

After ice volume corrections, there are no clear G/IG cycles for both $\delta^{18}O_{w-ivc}$ timeseries (**Figure 2e, f**). Surface seawater $\delta^{18}O_{w-ivc}$ shows significant positive values of 0.5-1.0 ‰ during MIS 6, 7, and 11 (**Figure 2e**). The $\delta^{18}O_{w-ivc}$ data of the subsurface water varies within 1.0 ‰ across the whole study period (**Figure 2f**). Only one positive excursion of ~1.2‰ is found at MIS 7e resulted from a subsurface strong warming.

4.5 Time series analyses

4.5.1 Spectra

Significant orbital cycles of eccentricity (100-kyr), obliquity (41-kyr) and precession (19- to 23-kyr) are found in the time series of $\delta^{18}O_c$ and temperature (**Table. 1; Figure 3**). Interestingly, clear eccentricity and precession periods occur in the $\delta^{18}O_{w-}$

$_{ivc}$ time series for the surface and subsurface waters, but there is no significant obliquity period.

For ΔT record, a long-cyclicity of ~300 kyr may be biased by strong differences around 100 and 240 ka. Here we performed an Ensemble Empirical Mode Decomposition (EEMD, Huang et al., 1998) to ban pass the long periodicity (**Supplementary figure 6**). Single spectral result of ΔT after EEMD is shown in **Figure 3h**. Precession (23-kyr) and weak obliquity (41-kyr) are shown with a potential 63-kyr obliquity cycle (Berger, 1978).

4.5.2 Cross spectral analyses and phase relationships

Results of cross spectral analyses between proxies and inferred hydrological conditions are listed in **Table 1** and depicted in **Supplementary figure 7**. In the $\delta^{18}O_c$ and temperature data, both species show almost identical phase. Clear orbital periodicities are expressed in the $\delta^{18}O_{w\text{-}ivc}$ records of both surface and subsurface waters.

5. Discussion

5.1 Solomon Sea thermocline structure during the past 568 kyr

5.1.1 The 100-kyr glacial-interglacial cycles

Over the past 568 kyr, the most pronounced feature is the ~100-kyr G/IG cycles in both the surface and subsurface geochemical records (**Figures 2 and 3a-f**). The planktonic foraminifera $\delta^{18}O_c$ shows almost synchronous phasing with eccentricity as suggested by the nearby ODP Hole 1115B records (Chuang et al., 2018). The surface and subsurface temperature records lead eccentricity by 7.3 to 12.3 kyr which is similar to previous studies in the equatorial Pacific Ocean (Lea et al., 2000; Liu and Herbert, 2004). However, the surface-subsurface thermal and hydrological differences ($\Delta\delta^{18}O_c$,

ΔT, and $\Delta\delta^{18}O_w$, **Figures 4a-c**) in the Solomon Sea only show weak 100-kyr G/IG contrast. Although the ΔT and $\Delta\delta^{18}O_w$ both show 100-kyr cycles in the spectral analysis (**Supplementary figure 6c**, **Figure 3i**), the phase relationship between ΔT and eccentricity is not persistent through time. That is why we cannot obtain phase angle from cross spectral analysis (**Table 1**). The temperature records leading eccentricity and the unstable phase relationship between ΔT and eccentricity show that the 100-kyr cycles in the temperature records are not related to eccentricity, but to the changes of global glacial-interglacial conditions.

The temperature differences across the past 568 kyr in the Solomon Sea are relative stable and close to the modern differences (3-5 $^{\circ}C$, **Figure 1e**). There are relative increasing of ΔT during Termination II and V, but there are also decreasing trends during Termination III, IV, and VI. The highest and lowest thermal gradient both occur right after the glacial termination periods (~120 and 240 kyr). On the opposite, the $\Delta\delta^{18}O_w$ shows clear salinity contrast (~0.25 to 0.50‰) during the past six terminations (**Figure 4c**). This suggest, similar to modern observation (**Figure 1e**), the main and persistent stratification factor in the Solomon Sea during the terminations is the salinity differences rather than the thermal contrast between the surface and upper thermocline waters.

Figure 4 also shows that the main factor for stratification could vary during different interglacials. During the ΔT maxima periods of MIS 5e-5a (**Figure 4**), the ΔT is very large but the $\Delta\delta^{18}O_w$ is rather small, indicating the thermal contrast is more important for the stratification. It is similar during MIS 9e and 11c although to a less extent. Differently, during MIS 7e and 13, the temperature contrast is rather small and the salinity contrast is relatively large, indicating a more important role of salinity on

the stratification. Model simulations show that MIS 5, 9 and 11 are the warmest interglacials especially in the Southern Hemisphere (SH) and the low-latitudes over the last 800 kyr, while MIS 7 and 13 are the coolest over the last 600 kyr (Yin and Berger, 2012). Therefore, there seems a distinct difference in the main contributor of the stratification between the warm and cool interglacials in the southwestern WPWP region.

5.1.2 The 41-kyr cycles and obliquity forcing

On the obliquity band of variabilities, both the surface and subsurface $\delta^{18}O_c$ and temperatures show 41-kyr cycles, which lag obliquity by ~3.8 to 6.8 kyr (33.5º-60º on the phase wheels, **Supplemetary figure 7**, **Table 1**). This suggests an impact from high latitude and/or subtropical South Pacific gyre variabilities as reported by previous studies (Liu and Herbert, 2004; Pena et al., 2008; Lee and Poulsen, 2005; Lo et al., 2014a; Hollstein et al., 2018; 2020).

Filtering results show that both higher SST and UTT correspond high obliquity (**Figure 5a-b**). As large obliquity leads to high annual insolation in the high latitudes but leads to low insolation in the low latitudes (Berger et al., 2010, low-latitude insolation would not be the direct factor for SST increase during the high obliquity periods. Both physical simulation (Lee and Poulsen, 2005) and geochemical records from the west (Hollstein et al., 2018; Hollstein et al., 2020) and east (Pena et al., 2008) equatorial Pacific regions suggest that the latitudinal insolation gradient which is mainly controlled by obliquity would play a role. A higher insolation gradient due to a larger obliquity would cause higher transportation from subtropical South Pacific gyre to equatorial Pacific regions through the "oceanic tunneling" process (Lee and Poulsen, 2005; Pena et al., 2008). Relative warmer and higher salinity water are transported by

SEC and then "resurfacing" due to geographical topography changes (Qu et al., 2013). Thus, both the SST and UTT increase in the Solomon Sea region when obliquity is large.

For the surface and subsurface temperature and seawater oxygen isotope differences (**Figures 5d-e**, **7**, **Table 1**), lower ΔT and higher $\Delta\delta^{18}O_w$ correspond to large obliquity, although the $\Delta\delta^{18}O_w$ lags obliquity by ~6.2 kyr (124.9°. **Table 1**). This could be explained by the higher subtropical gyre transportation mechanism mentioned above.

5.1.3 The 23-kyr and 19-kyr cycles and precession forcing

The 23-kyr and 19-kyr cycles, which are the two main periodicities of the precession cycles (Berger, 1978), are clearly present in the geochemical proxies in the Solomon Sea except the $\Delta\delta^{18}O_c$ (**Figure 3**). This indicates a strong effect of precession on the thermal and hydrological conditions in the Solomon Sea during the past 568 kyr.

Figure 6b shows that the precession-band filtered SST has a high and negative correlation with precession, with higher SST corresponding to precession minimum and vice versa. This is in agreement with the results of the transient simulations which show a strong and negative relationship between precession and the annual temperature in the SH tropics (Yin and Berger, 2015). **Figure 6c** and **d** shows that higher UTT and lower ΔT also correspond to precession minimum. HadCM3 sensitivity experiments show that in response to precession minimum, the thermocline in the western tropical Pacific is deepened (Karami et al., 2015). The higher UTT and lower ΔT at precession minimum could thus be either induced by the deepening of the mixed layer and/or stronger subtropical SEC branch transportation through the south entrance of the Solomon Sea (**Figure 1**).

Both high subsurface $\delta^{18}O_{w\text{-}ivc}$ and $\Delta\delta^{18}O_w$ also correlate well with precession minimum with minor time lag (0.8 to 3.3 kyr, **Supplementary figure 7, Table 1**). Simulation results suggest high insolation induced by precession minimum could promote asymmetric wind field near equator (Clement, 1999; 2000), and a La Niña-like condition was simulated in response to precession minimum (Pena et al., 2008; Karami et al., 2015). Although the deepening of the mixed layer shall also strengthen the vertical mixing in the Solomon Sea and further transport the fresher surface water signal to the subsurface water depth where *P. obliquiloculata* live. However, according to the modern salinity profile in the Solomon Sea (**Figure 1e**), the dominance of low salinity fresher surface water only occupies a very shallow depth of 0-25 m. The majority of the subsurface salinity is still controlled by the high salinity core, which maximum is located around 200-300 m. Therefore, the subsurface $\delta^{18}O_{w\text{-}ivc}$ and $\Delta\delta^{18}O_w$ could also be explained by the deepening of the mixed layer.

5.1.4 Terminations

In order to further examine in detail of the G/IG transitions in the Solomon Sea, we align all the surface and subsurface temperatures and hydrological records over the past 6 terminations in **Figure 8**. The reference timing (here "0") refers to the MIS boundaries proposed by Lisiecki and Raymo (2005). Regarding the thermal structure evolution, the surface and upper thermocline waters both show an early warming (3-5 kyr) before the terminations. During Termination II, III, and IV, the peak interglacial thermal maxima are reached within +2 to +4 kyr from the G/IG boundaries, and they are clearly delayed by +6 to +8 kyr during Termination I, V, and VI. For the hydrological parameters, the subsurface $\delta^{18}O_{w\text{-}ivc}$ shows a major positive excursion during the termination periods, although the timings are slightly different. Termination

I, III, V, and VI have major positive excursions right at the termination. Termination IV shows earlier (~6 kyr) positive seawater oxygen isotope excursion, and Termination II shows a long and slightly positive value across the termination period (-6 to +12 kyr) (**Figure 8c, d**). Complex patterns are observed in the surface water hydrological conditions during terminations. Lo et al. (2014a) reported that the surface hydrological records mostly respond to precipitation movements during the Termination I and this observation still holds in Termination II and V (Cheng et al., 2009; Cheng et al., 2016). However, details are difficult to capture on the millennial timescale regarding the mean sea level corrections (**Supplementary figure 3**). For the duration of each peak interglacial period, the surface waters show longer warm periods than subsurface water only in Termination II and IV, but not the other deglaciations. This observation further shows the differences between individual G/IG cycles in the Solomon Sea region.

Termination V (MIS 12-11) is the most special case in the Solomon Sea during the past 568 kyr. First, both SST and UTT show very early and persistent warming without millennial timescale perturbation since 10-12 kyr before the termination. The lack of millennial timescale interruption during Termination V are also found in other studies (Barker et al., 2021; Rohling et al., 2010). Second, the thermal maximum in the Solomon Sea during MIS 11 was reached until 14-18 kyr after Termination V. The $\delta^{18}O_C$ of both the surface and upper thermocline dwellers show a pattern similar to the global benthic stack, and reach peak interglacial values right after the termination followed by a plateau pattern lasting for ~20 kyr (**Figure 2a, 2b**). In consequence, long and steady positive seawater oxygen isotope excursions are observed in both the surface and subsurface waters (**Figure 2e, f**; **Supplementary figure 3a, b**). An exceptionally long MIS 11 has also been confirmed by transient climate simulations, and it has been demonstrated to relate to the long-lasting low eccentricity and high CO_2 concentration

as well as the anti-phase relationship between obliquity and precession (Yin and Berger, 2015). The early warming of Termination V starts from 435-437 ka (surface and subsurface water, respectively), a timing when precession starts to decrease and obliquity starts to increase. As aforementioned, the surface and subsurface temperatures in the Solomon Sea are negatively correlated with precession and positively correlated with obliquity, the precession decrease and obliquity increase from 437 kyr would lead to the early warming. In addition, CO_2 also starts to increase at the same time (~435 kyr BP), which could also contribute to the early warming.

5.2 The role of orbital forcing on the regional ocean circulation

On the orbital timescale, both SST and UTT positively correlate to obliquity and negatively correlate to precession (high temperatures with high tilt angle and low precession, **Figures 5b, 5c, 6b, 6c**). A clear dominance of precessional pacing and related subtropical-equatorial vertical water column structure changes during the past several G/IG cycles has been demonstrated by several studies in the western pacific equatorial regions (Jian et al., 2020; Zhang et al., 2021) and this study as well, although a study suggests eccentricity dominated hydroclimate in Indonesia (Ulfers et al., 2021). Either through the seasonal surface-subsurface water transportation via different sources (Jian et al. 2020) or through a series atmospheric-oceanic dynamic transportation (Zhang et al., 2021, **Figure 9**), precession-induced insolation change is a strong candidate mechanism for the variations of equatorial climate changes especially on the orbital timescale, as also shown in model simulations (Yin and Berger, 2015).

Obliquity also plays an important role on the middle-high to low latitude insolation gradients and on the heat transportation from tropical to higher latitudes through the

subtropical South Pacific oceanic tunnelling (Hollstein et al., 2018; 2020; Lee and Poulsen, 2005; Pena et al., 2008; Qu et al., 2013). The reconstructed Solomon Sea thermal and hydrological records mostly show obliquity and precessional cycles which are similar to the pattern in the equatorial and southwestern Pacific regions (Pena et al., 2008; Pahnke et al., 2003, **Supplementary figure 4**).

Here we further examine the regional differences of hydrological-thermal condition response to orbital forcing by comparing our Solomon (9°S) and central equatorial records (KX97322-4, Zhang et al., 2021) during the past 350 kyr. Results show generally similar G/IG pattern for the subsurface temperatures (**Figure 9a, b**) and $\delta^{18}O_w$ (**Figure 9c, d**) records. A stronger Solomon Sea SST variability in amplitude is a clear difference from the central equatorial Pacific Ocean. Consequently, the vertical temperature gradient in the central equatorial Pacific Ocean is dominated by subsurface temperature variations (**Figure 9e**). In the $\Delta\delta^{18}O_{w\text{-}ivc}$ comparison, a significant obliquity periodicity can also be observed in the Solomon Sea but not in the KX97322-4 records (spectral analysis results from their figure 2i), although the records seem very similar to each other (**Figure 9f**).

Clear obliquity signal in both the surface and subsurface records in the Solomon Sea indicates an influence of the subtropical gyre and the high latitude climate through the oceanic tunneling and/or re-surfacing process suggested by numerical modelling and modern observations (Liu and Herbert, 2004; Pena et al., 2008; Lee and Poulsen, 2005; Qu et al., 2013). Persistent precession pacing in both SST and UTT is a common reflection of low-latitude forcing in both central and southwestern equatorial Pacific Ocean revealed by these comparisons.

6. Concluding remarks

Here we present high-resolution vertical water column thermal and hydrological records for the Solomon Sea during the past 568 kyr. The SST and UTT show 4 to 6 $^{\circ}$C difference between glacial and interglacial periods. The variabilities of the thermal (ΔT: 2 to 4 $^{\circ}$C) and hydrological ($\Delta\delta^{18}O_{w\text{-}ivc}$: 0 to 1 ‰) water structures suggest a relatively persistent influence of the SEC and subtropical gyre circulation. The subsurface $\delta^{18}O_{w\text{-}ivc}$ shows a clear positive excursion ~0-6 kyr before the terminations, while the surface water $\delta^{18}O_{w\text{-}ivc}$ shows rather complex patterns during the past six terminations. The early (12 to 18 kyr before the termination) and persistent warming during Termination V in both the surface and subsurface water temperatures are different from the "rapid warming then cooling" pattern during other terminations.

Our results show strong subsurface salinity variabilities on multiple orbital and even millennial timescales, although the overall water stratification could be muted by complex SST response to both insolation and local circulations. They also show that the subsurface temperature variabilities are controlled by both South subtropical gyre transportation and the deepening of mixed layer. We also confirm the importance of the role of subsurface water in local to regional water thermal and hydrological stratifications.

On the obliquity band, larger obliquity leads to higher SST and UTT at the Solomon Sea, suggesting higher subtropical South Pacific input. This is also supported by lower ΔT and higher $\Delta\delta^{18}O_w$. In the meantime, precession minimum also leads to higher SST and UTT, suggesting an expansion of the mixed layer with lower ΔT and

greater $\Delta\delta^{18}O_w$. Our results suggest complex interactions between precipitation-evaporation and water masses exchange in the Solomon Sea.

To sum up the vertical water column structure variations over the past 568-kyr in the Solomon Sea, we find that **1.** strong subsurface salinity signal on orbital and even millennial timescales, although the overall water stratification could be muted by SST in the complex response to both insolation and local circulation. **2.** subsurface temperature variabilities are controlled both by South subtropical gyre transportation and the deepening of mixed layer. Overall, the clear obliquity pacing observed in the SST, UTT, ΔT and $\Delta\delta^{18}O_w$ records would suggest strong interactions between the Solomon Sea and the mid-high latitude South Pacific regions. We also confirm the importance of the role of subsurface water in local to regional water thermal and hydrological stratifications.

The regional comparison between the central equatorial and southwestern Pacific Ocean suggests dominant precession pacing but the role of obliquity is persistent and significant as well. The clear obliquity pacing observed in our SST, UTT, ΔT and $\Delta\delta^{18}O_w$ records would suggest strong interactions between the Solomon Sea and the mid-high latitude South Pacific regions. However, two questions remain unclear and need further investigation: (1) Why does the obliquity signal disappear in the central equatorial region if the gyre circulation keeps transporting subsurface water through the Solomon Sea to central equatorial Pacific Ocean? (2) Why are the SST and UTT strongly coupled through the G/IG cycles in the southwest equatorial Pacific Ocean but not in the central Pacific Ocean region? Based on the new dataset and mechanism presented in this study, we speculate the existence of a strong barrier and/or dilution between the South Pacific to equator and North Pacific Ocean regions during the past

5-6 G/IG cycles. Also, relatively short span (mostly < 200 kyr) of many records from the equatorial and North Pacific regions may prohibit the detection of the obliquity signal. We also suggest that the subsurface $\delta^{18}O_{w-ivc}$ could be a good indicator of high salinity water mass from South Pacific subtropical region. On longer timescale, there were clear subsurface water mass change induced subsurface seawater oxygen isotope variabilities in the western Indian Ocean (Karas et al., 2009, 2011). These studies suggest that warm-saline subsurface water from the South Pacific Ocean plays an important role in the past climate changes and global thermohaline circulations.

Another important question that deserves future investigation is what are the impacts of greenhouse gases and ice sheets on the equatorial Pacific thermal and hydrological conditions in comparison to orbital forcing and to which extent they indirectly contribute to the "orbital cycles" observed in the records. High resolution vertical water column records with longer time span in the equatorial Pacific region and coupled physical climate simulation are crucial to understand how the equatorial thermal-hydrological processes respond to different climatic forcings.

Authors contribution:

Authors' contributions are listed below: L.L. and C.C.S. designed the study. C.Z. and Y.H.T. performed time-series analyses. C.C.Y., T.L.C., Y.C.S., C.K.C., and Y.C.C. picked samples. L.L., C.C.Y., T.L.C., Y.C.S., H.S.M., C.K.C., and Y.C.C. performed oxygen isotope and Mg/Ca ratios. L.L. and C.K.C. established age model. L.L. and C.C.Y. prepared figures. L.L. prepared the first draft and all authors polished and improved the manuscript.

References

Anand, P., Elderfield, H., Conte, M., 2003. Calibration of Mg/Ca thermometry in planktonic foraminifera from a sediment trap time series. Paleoceanography 18. https://doi.org/10.1016/j.epsl.2008.06.029.

Barker, S., Knorr, G., Conn, S., Lordsmith, S., Newman, D., Thornalley, D., 2021. Early interglacial legacy of deglacial climate instability. Paleoceanography and Paleoclimatology, 34, 1455-1475. https://doi.org/10.1029/2019PA003661.

Bemis, B.E., Spero, H.J., Bijma, J., Lea, D.W., 1998. Reevaluation of the oxygen isotopic composition of planktonic foraminifera: Experimental results and revised paleotemperature equations. Paleoceanography 13, 150-160. https://doi.org/10.1029/98PA00070.

Berger, A., 1978. Long-term variations of daily insolation and quaternary climatic changes. Journal of Atmospheric Sciences 35, 2362–2367

Berger A., Loutre M.F., and Yin Q.Z., 2010. Total irradiation during any time interval of the year using elliptic integrals. Quaternary Science Reviews, 29, 1968-1982.

Boillet, T., Hollbourn, A., Kuhnt, W., Laj, C., Kissel, C., Beaufort, L., Kienast, M., Andersen, N., Garbe-Schönberg, D., 2011. Mindanao Dome variability over

the last 160 kyr: Episodic glacial cooling of the West Pacific Warm Pool. Paleoceanography 26, PA1208.

Cane, M.A., 1988. Climate change: a role for the tropical Pacific. Science 282, 59–61.

Cheng, H., Edwards, L., Broecker, W.S., Denton, G.H., Kong, X., Wang, Y., Zhang, R., Wang, X., 2009. Ice age terminations. Science 326, 248-252.

Cheng, H., Edwards, R.L., Sinha, A., Spötl, C., Yi, L., Chen, S., Kelly, M., Kathayat, G., Wang, X., Li, X., Kong, X., Wang, Y., Ning, Y., Zhang, H., 2016. The Asian monsoon over the past 640,000 years and ice age terminations. Nature 534, 640-646. https://doi:10.1038/nature18591

Chuang, C.-K., Lo, L., Zeeden, C., Chou, Y.-M., Wei, K.-Y., Shen, C.-C., Mii, H.-S., Chang, Y.-P., Tung, Y.-H., 2018. Integrated stratigraphy of ODP Site 1115 (Solomon Sea, southwestern equatorial Pacific) over the past 3.2 Ma. Marine Micropaleontology 144, 25-37.

Clement, A.C., Seager, R., Cane, M.A., 1999. Orbital controls on the El Niño/Southern Oscillation and the tropical climate. Paleoceanography 14, 441-456.

Clement, A.E., Seager, R., Cane, M.A., 2000. Suppression of El Niño during the mid-Holocene by changes in the Earth's orbit. Paleoceanography 15, 731-737.

Cravatte, S., Delcroix, T., Zhang, D., McPhaden, M., Leloup, J., 2009. Observed freshening and warming of the western Pacific warm pool. Climate Dynamics 33, 565-589. https://doi.org/10.1007/s00382-009-0526-7.

Cravatte, S., Ganachaud, A., Duong, Q.-P., Kessler, W.S., Eldin, G., Dutrieux, P., 2011. Observed circulation in the Solomon Sea from SADCP data. Progress in Oceanography 88, 116-130. https://doi.org/10.1016/j.pocean.2010.12.015.

Dang, H., Jian, Z., Bassinot, F., Qiao, P., Cheng, X., 2012. Decoupled Holocene variability in surface and thermocline water temperatures of the Indo-Pacific Warm Pool. Geophysical Research Letters 39. https://doi.org/10.1029/2011GL050154.

Dang, H., Jian, Z., Wu, J., Bassinot, F., Wang, T., Kissel, C., 2018. The calcification depth and Mg/Ca thermometry of *Pulleniatina obliquiloculata* in the tropical Indo-Pacific: A core-top study. Marine Micropaleontology 145, 28-40. https://doi.org/10.1016/j.marmicro.2018.11.001.

Dang, H., Jian, Z., Wang, Y., Mohtadi, M., Rosenthal, Y., Ye, L., Bassinot, F., Kuhnt, W., 2020. Pacific warm pool subsurface heat sequestration modulated Walker circulation and ENSO activity during the Holocene. Science Advances 6, eabc0402. https://doi.org/10.1126/sciadv.abc0402.

de Garidel-Thoron, T., Rosenthal, Y., Bassinot, F., Beaufort, L., 2005. Stable sea surface temperatures in the western Pacific warm pool over the past 1.75 million years. Nature 433, 294-298.

Ford, H., McChesney, C., Hertzberg, J., McManus, J., 2018. A deep eastern equatorial Pacific thermocline during the Last Glacial Maximum. Geophysical Research Letters 45, 11,806-811,816. https://doi.org/10.1029/2018GL079710.

Ganachaud, A., Cravatte, S., Melet, A., Schiller, A., Holbrook, N., Sloyan, B., Widlansky, M., Bowen, M., Verron, J., Wiles, P., 2014. The Southwest Pacific Ocean circulation and climate experiment (SPICE). Journal of Geophysical Research: Oceans 119, 7660-7686. https://doi.org/10.1002/2013JC009678.

Ganachaud, A., Cravatte, S., Sprintall, J., Germineaud, C., Alberty, M., Jeandel, C., Eldin, G., Metzl, N., Bonnet, S., Benavides, M., 2017. The Solomon Sea: its circulation, chemistry, geochemistry and biology explored during two oceanographic cruises. Elementa: Science of the Anthropocene 5. https://doi.org/10.1525/elementa.221.

Gasparin, F., Ganachaud, A., Maes, C., Marin, F., Eldin, G., 2012. Oceanic transports through the Solomon Sea: The bend of the New Guinea coastal undercurrent. Geophysical Research Letters 39. https://doi.org/10.1029/2012GL052575.

Germineaud, C., Ganachaud, A., Sprintall, J., Cravatte, S., Eldin, G., Alberty, M.S., Privat, E., 2016. Pathways and water mass properties of the thermocline and intermediate waters in the Solomon Sea. Journal of Physical Oceanography 46, 3031-3049. https://doi.org/10.1175/JPO-D-16-0107.1.

Germineaud, C., Cravatte, S., Sprintall, J., Alberty, M., Grenier, M., Ganachaud, A., 2021. Deep pacific circulation: New insights on pathways through the Solomon Sea. Deep Sea Research Part I: Oceanographic Research Papers 171, 103510. https://doi.org/10.1016/j.dsr.2021.103510.

Grenier, M., Cravatte, S., Blanke, B., Menkes, C., Koch-Larrouy, A., Durand, F., Melet, A., Jeandel, C., 2011. From the western boundary currents to the Pacific Equatorial Undercurrent: Modeled pathways and water mass evolutions. Journal of Geophysical Research: Oceans 116. https://doi.org/10.1175/JPO-D-16-0107.1.

Grenier, M., Jeandel, C., Cravatte, S., 2014. From the subtropics to the equator in the Southwest Pacific: Continental material fluxes quantified using neodymium data along modeled thermocline water pathways. Journal of Geophysical Research: Oceans 119, 3948-3966. https://doi.org/10.1002/2013JC009670.

Hol1stein, M., Mothadi, M., Rosenthal, Y., Prange, M., Oppo, D.W., Mendez, G.M., Tachikawa, K., Sanchez, P.M., Steinke, S., Hébbln, D., 2018. Variations in Western Pacific War, Pool surface and thermocline conditions over the past 110,000 years: Forcing mechanisms and implications for glacial Walker circulation. Quaternary Science Reviews 201, 429-445.

Hollstein, M., Mothadi, M., Kienast, M., Rosenthal, Y., Groenveld, J., Oppo, D.W., Southon, J.R., Lückge, A., 2020. The impact of Astronomical forcing on surface and thermocline variability within the Western Pacific Warm Pool over the past 160 kyr. Paleoceanography and Paleoclimatology 35, e2019PA003832. https://doi.org/10.1029/2019PA003832.

Howell, P., Pisias, N., Balance, J., Baughman, J., Ochs, L., 2006. ARAND time-series analysis software, Brown University, Providence RI.

Huang, N.E., Shen, Z., Long, S.R., Wu, M.C., Shih, H.H., Zheng, Q., Yen, N.-C., Tung, C.C., Liu, H.H., 1998. The empirical mode decomposition and the Hilbert spectrum for nonlinear and non-stationary time series analysis. Proceedings of the Royal Society A: Mathematical, Physical and Engineering Sciences 454, 903-995.

Jian, Z., Wang, Y., Dang, H., Lea, D.W., Liu, Z., Jin, H., Yin, Y., 2020. Half-precessional cycle of thermocline temperature in the western equatorial Pacific and its bihemispheric dynamics. Proceedings of the National Academy of Sciences 117, 7044-7051. https://doi.org/10.1073/pnas.1915510117.

Karami, M.P., Herold, N., Berger, A., Yin, Q.Z., Muri, H., 2015. State of the tropical Pacific Ocean and its enhanced impact on precipitation over East Asia during Marine Isotopic Stage 13. Climate Dynamics, 44, 807–825, doi 10.1007/s00382-014-2227-0.

Karas, C., Nürnberg, D., Gupta, A.K., Tiedemann, R., Mohan, K., Bickert, T., 2009. Mid-Pliocene climate change amplified by a switch in Indonesian subsurface through flow.

Karas, C., Nürnberg, D., Tiedemann, R., Garbe-Schönberg, D., 2011. Pliocene climate change of the Southwest Pacific and the impact of ocean gateways. Earth and Planetary Science Letters 301, 117-124.

Lakhani, K.Q., Lynch-Stieglitz, J., Monteagudo, M.M., 2022. Constraining calcification habitat using oxygen isotope measurements in tropical planktonic foraminiferal tests from surface sediments. Marine Micropaleontology 170, 102074. https://doi.org/10.1016/j.marmicro.2021.102074

Laskar, J., Robutel, P., Joutel, F., Gastineau, M., Correia, A., Levrard, B., 2004. A long-term numerical solution for the insolation quantities of the Earth. Astronomy & Astrophysics 428, 261-285. https://doi.org/10.1051/0004-6361:20041335.

Lea, D.W., Pak, D.K., Spero, H.W., 2000. Climate impact of late Quaternary equatorial Pacific sea surface temperature variations. Science 289, 1719-1724.

Lee, S.-Y., and Poulsen, C.J., 2005. Tropical Pacific climate response to obliquity forcing in the Pleistocene. Paleoceanography 20, PA4010. https://doi:10.1029/2005PA001161.

Lisiecki, L.E., Raymo, M.E., 2005. A Pliocene-Pleistocene stack of 57 globally distributed benthic $\delta^{18}O$ records. Paleoceanography 20. https://doi.org/10.1029/2004PA001071.

Liu, Z., Herbert, T.D., 2004. High-latitude influence on the eastern equatorial Pacific climate in the early Pleistocene epoch. Nature 427, 720-723.

Liu, Y., Lo, L., Shi, Z., Wei, K.-Y., Chou, C.-J., Chen, Y.-C., Chuang, C.-K., Wu, C.-C., Mii, H.-S., Peng, Z., 2015. Obliquity pacing of the western Pacific Intertropical Convergence Zone over the past 282,000 years. Nature communications 6, 1-7. https://doi.org/10.1038/ncomms10018.

Lo, L., Chang, S.-P., Wei, K.-Y., Lee, S.-Y., Ou, T.-H., Chen, Y.-C., Chuang, C.-K., Mii, H.-S., Burr, G.S., Chen, M.-T., 2017. Nonlinear climatic sensitivity to greenhouse gases over past 4 glacial/interglacial cycles. Scientific reports 7, 1-7. https://doi.org/10.1038/s41598-017-04031-x.

Lo, L., Lai, Y.-H., Wei, K.-Y., Lin, Y.-S., Mii, H.-S., Shen, C.-C., 2013. Persistent sea surface temperature and declined sea surface salinity in the northwestern tropical Pacific over the past 7500 years. Journal of Asian Earth Sciences 66, 234-239. https://doi.org/10.1016/j.jseaes.2013.01.014.

Lo, L., Shen, C.-C., Wei, K.-Y., Burr, G., Mii, H.-S., Chen, M.-T., Lee, S.-Y., Tsai, M.-C., 2014a. Millennial meridional dynamics of the Indo-Pacific Warm Pool during the last termination. Climate of the Past 10, 2253-2261. https://doi.org/10.5194/cp-10-2253-2014.

Lo, L., Shen, C.-C., Lu, C.-J., Chen, Y.-C., Chang, C.-C., Wei, K.-Y., Qu, D., Gagan, M.K., 2014b. Determination of element/Ca ratios in foraminifera and corals using cold-and hot-plasma techniques in inductively coupled plasma sector field mass spectrometry. Journal of Asian Earth Sciences 81, 115-122. https://doi.org/10.1016/j.jseaes.2013.11.016.

Locarnini, R.A., Mishonov, A.V., Antonov, J.I., Boyer, T.P., Garcia, H.E., 2006. World Ocean Atlas 2005, Volume 1: Temperatures. S. Levitus, Ed. NOAA Atlas NESDIS 61, U.S. Government Printing Office, Washington, D.C., 182 pp.

Mohtadi, M., Prange, M., Oppo, D.W., De Pol-Holz, R., Merkel, U., Zhang, X., Steinke, S., Lückge, A., 2014. North Atlantic forcing of tropical Indian Ocean climate. Nature 509, 76-80.

Nascimento, R., Venancio, I., Chiessi, C., Ballalai, J., Kuhnert, H., Johnstone, H., Santos, T., Prange, M., Govin, A., Crivellari, S., 2021. Tropical Atlantic stratification response to late Quaternary precessional forcing. Earth and Planetary Science Letters 568, 117030. https://doi.org/10.1016/j.epsl.2021.117030.

Pahnke, K., Zahn, R., Elderfield, H., Schulz, M., 2003. 340,000-year centennial-scale marine record of southern hemisphere climatic oscillation. Science 301, 948-952.

Paillard, D., Labeyrie, L., Yiou, P., 1996. Macintosh program performs time-series analysis, Eos Trans. AGU 77, 379.

Pang, X., Bassinot, F., Sepulcre, S., 2021. Indonesian Throughflow variability over the last two glacial-interglacial cycles: Evidence from the eastern Indian Ocean. Quaternary Science Reviews 256, 106839. https://doi.org/10.1016/j.quascirev.2021.106839.

Pena, L., Cacho, I., Ferretti, P., Hall, M., 2008. El Niño–Southern Oscillation–like variability during glacial terminations and interlatitudinal teleconnections. Paleoceanography 23. https://doi.org/10.1029/2008PA001620.

Qu, T., Gao, S., Fine, R.A., 2013. Subduction of south Pacific tropical water and its equatorward pathways as shown by a simulated passive tracer. Journal of physical oceanography 43(8), 1551-1565. https://doi.org/10.1175/JPO-D-12-0180.1

Railsback, L.B., Gibbard, P.L., Head, M.J., Voarintsoa, N.R.G., Toucanne, S., 2015. An optimized scheme of lettered marine isotope substages for the last 1.0 million years, and the climatostratigraphic nature of isotope stages and substages. Quaternary Science Reviews 111, 94-106.

Rohling, E.J., Braun, K., Grant, K., Kucera, M., Roberts, A.P., Siddall, M., Trommer, G., 2010. Comparison between Holocene and Marine Isotope Stage-11 sea-level histories. Earth and Planetary Science Letters 291, 97-105.

Rustic, G.T., Polissar, P.J., Ravelo, A.C., White, S.M., 2020. Modulation of late Pleistocene ENSO strength by the tropical Pacific thermocline. Nature communications 11, 1-11. https://doi.org/10.1038/s41467-020-19161-6.

Schlitzer, R., 2021. Ocean data view, http://odv.awi.de.

Schulz, M., Mudelsee, M., 2002. REDFIT: Estimating red-noise spectra directly from unevenly spaced paleoclimatic time series. Computers and Geosciences 28, 421-426.

Spratt, R.M., Lisiecki, L.E., 2016. A Late Pleistocene sea level stack. Climate of the Past 12, 1079-1092. https://doi.org/10.5194/cp-12-1079-2016.

Tachikawa, K., Cartapanis, O., Vidal, L., Beaufort, L., Barlyaeva, T., Bard, E., 2012. The precession phase of hydrological variability in the Western Pacific Wark Pool during the past 400 ka. Quaternary Science Reviews 30, 3716-3727.

Ulfers, A., Hesse, K., Zeeden, C., Russell, J.M., Vogel, H., Bijaksana, S., Wonik, T., 2021. Cyclostratigraphy and paleoenvironmental inference from downhole

logging of sediments in tropical Lake Towuti, Indonesia. Journal of Paleolimnology 65, 377-392.

Wang, X., Jian, Z., Lückge, A., Wang, Y., Dang, H., Mohtadi, M., 2018. Precession-paced thermocline water temperature changes in response to upwelling conditions off southern Sumatra over the past 300,000 years. Quaternary Science Reviews 192, 123-134. https://doi.org/10.1016/j.quascirev.2018.05.035.

Wara, M.W., Ravelo, A.C., Delaney, M.L., 2005. Permanent El Niño-like conditions during the Pliocene warm period. Science 309, 758-761. https://doi.org/10.1126/science.1112596

Weiss, T.L., Linsley, B.K., Gordon, A.L., 2021. Pacific North Equatorial Current bifurcation latitude and Kuroshio Current shifts since the Last Glacial Maximum inferred from a Sulu Sea thermocline reconstruction. Quaternary Science Reviews 264, 106999. https://doi.org/10.1016/j.quascirev.2021.106999.

Xu, J., Holbourn, A., Kuhnt, W., Jian, Z., Kawamura, H., 2008. Changes in the thermocline structure of the Indonesian outflow during Terminations I and II. Earth and Planetary Science Letters 273, 152-162. https://doi.org/10.1016/j.epsl.2008.06.029.

Xu, J., Kuhnt, W., Holbourn, A., Regenberg, M., Andersen, N., 2010. Indo-Pacific warm pool variability during the Holocene and Last Glacial Maximum. Paleoceanography 25. https://doi.org/10.1029/2010PA001934

Yin, Q., and Berger, A., 2012. Individual contribution of insolation and CO_2 to the interglacial climates of the past 800,000 years. Climate Dynamics 38, 709-724. doi: 10.1007/s00382-011-1013-5.

Yin, Q., and Berger, A., 2015. Interglacial analogues of the Holocene and its natural near future. Quaternary Science Reviews, 120, 28-46. https://doi.org/10.1016/j.quascirev.2015.04.008.

Zhang, P., Xu, J., Holbourn, A., Kuhnt, W., Beil, S., Li, T., Xiong, Z., Dang, H., Yan, H., Pei, R., Ran, Y., Wu, H., 2020. Intertropical Convergence Zone: Discrepancy on Precession and Obliquity Bands over the last 410 kyr. Journal of Geophysical Research: Atmospheres 125, e2019JD032125. https://doi.org/10.1029/2019JD032125.

Zhang, S., Yu, Z., Gong, X., Wang, Y., Chang, F., Lohmman, G., Qi, Y., Li, T., 2021. Precession cycles of the El Niño/Southern oscillation-like system controlled by Pacific upper-ocean stratification. Communications earth and environment 2, 239. https://doi.org/10.1038/s43247-021-00305-5.

Figures and captions
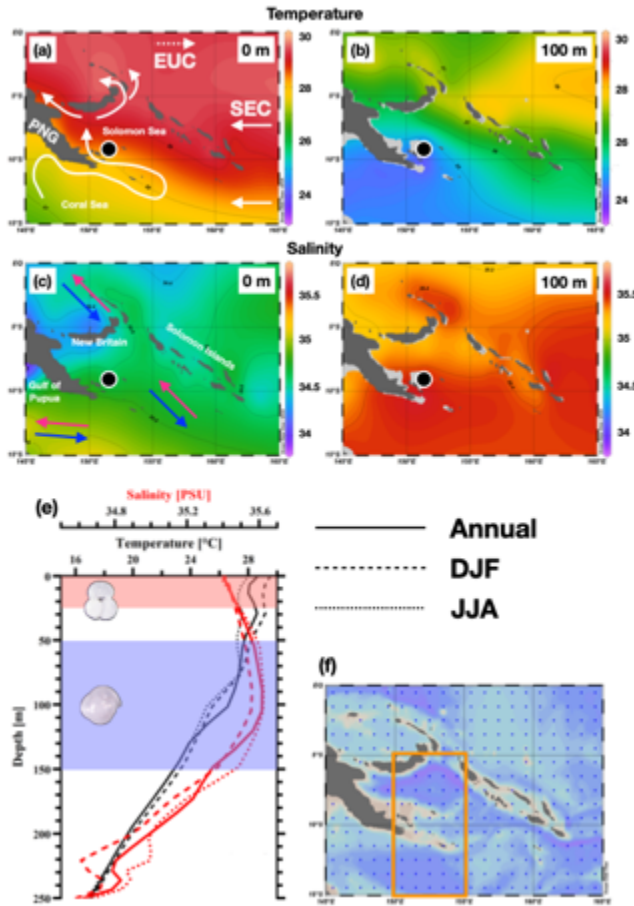
Figure 1. Maps of annual mean temperature (a, b) and salinity (c, d) for surface (0-m, a, c) and upper thermocline (100-m, b, d) layers. Annual and seasonal vertical temperature and salinity profiles averaged over the orange box (f) is presented in (e). White solid and dashed arrows in (a) are schematic flow directions of south equatorial current (SEC) and equatorial undercurrent (EUC) near the Papua New Guinea (PNG) region, respectively. Pink and blue solid arrows in (c) are schematic wind directions in July and January, respectively. Black dot denotes the location of site MD05-2925 (Data from World Ocean Atlas; Locarnini et al., 2006).
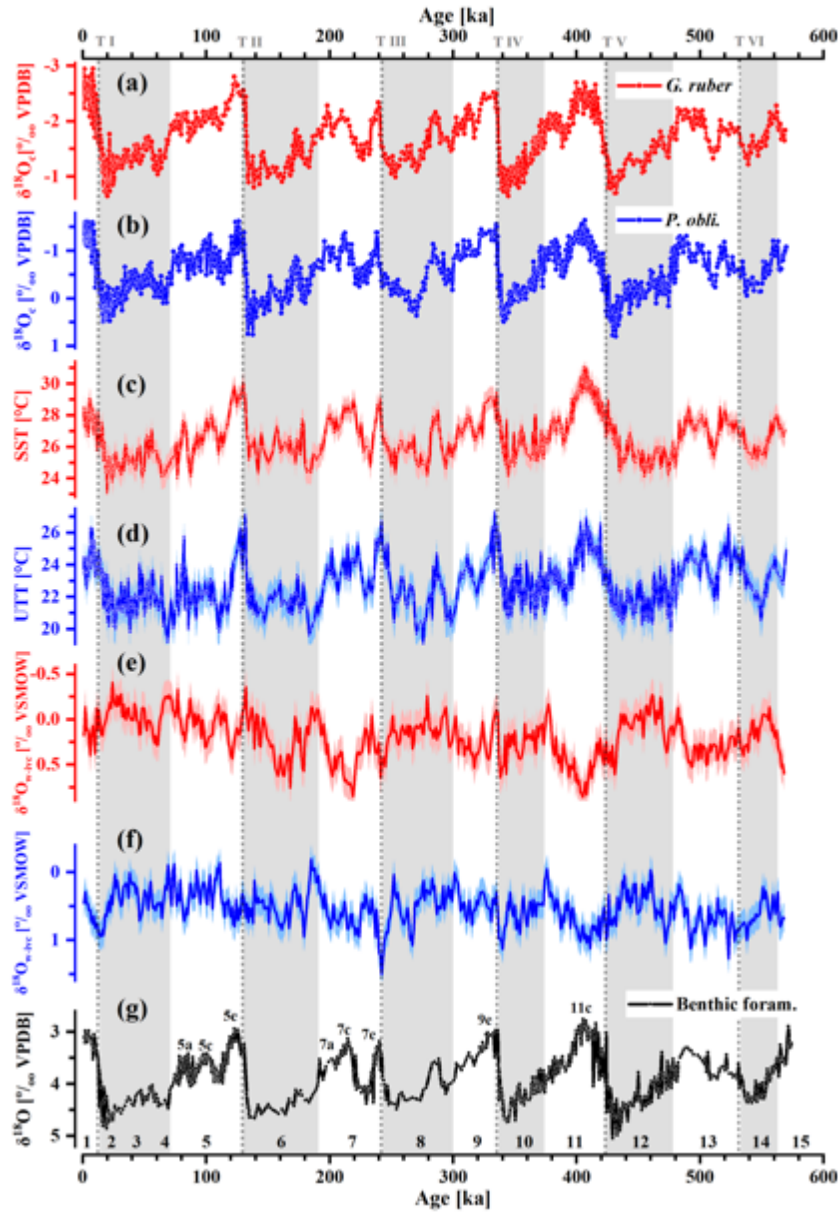
Figure 2. Paleoclimate records and age model of MD05-2925. Carbonate $\delta^{18}O$ ($\delta^{18}O_C$) of (a) *G. ruber* and (b) *P. obliquiloculata*. Mg/Ca ratios inferred (c) sea surface and (d) upper thermocline temperatures (SST and UTT). Ice volume corrected surface (e, red) and subsurface (f) sea water oxygen isotope ($\delta^{18}O_{w-ivc}$). MD05-2925 composite benthic foraminiferal oxygen isotope records (g, black). Light gray bars and dotted gray lines are glacial periods and major glacial terminations, respectively. Marine isotope stage (MIS) and substages are listed according to Lisiecki and Raymo (2005) and Railsback et al. (2015). Envelopes color shading in c-f indicate 1σ error followed Mohtadi et al. (2014) method.
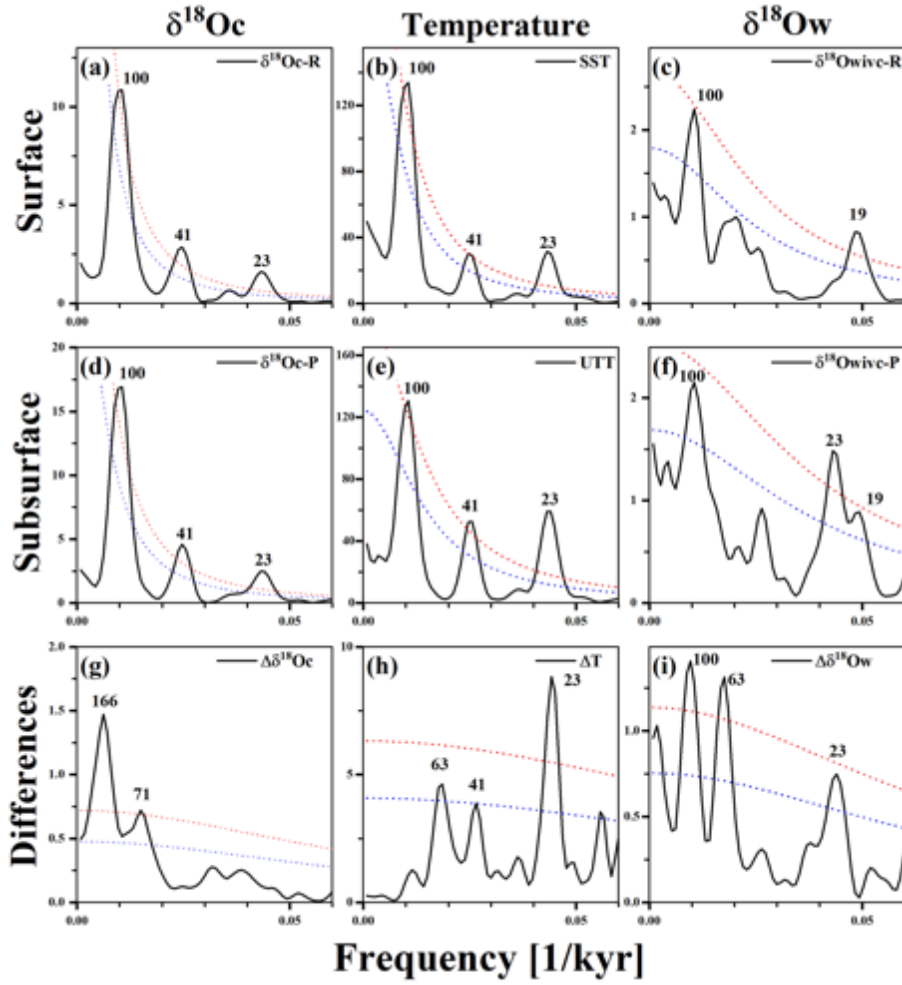
Figure 3. Single spectrum spectral results of foraminiferal geochemical proxies. (a) Carbonate $\delta^{18}O$ ($\delta^{18}O_C$), (b) inferred sea surface temperature (SST), and (c) ice-volume-corrected seawater $\delta^{18}O$ ($\delta^{18}O_{w\text{-}ivc}$) of *G. ruber*. (d) $\delta^{18}O_C$, (e) inferred upper thermocline temperature (UTT), and (f) $\delta^{18}O_{w\text{-}ivc}$ of *P. obliquiloculata*. Inter-species differences of (g) $\Delta\delta^{18}O_C$, inferred (h) ΔT and (i) seawater oxygen isotope ($\Delta\delta^{18}O_w$). Red and blue dashed lines are 95% and 80% confidence lines, respectively. Note that ΔT single spectrum results are derived from Ensemble Empirical Mode Decomposition (EEMD, Huang et al., 1998; **Supplementary Figure 6**).
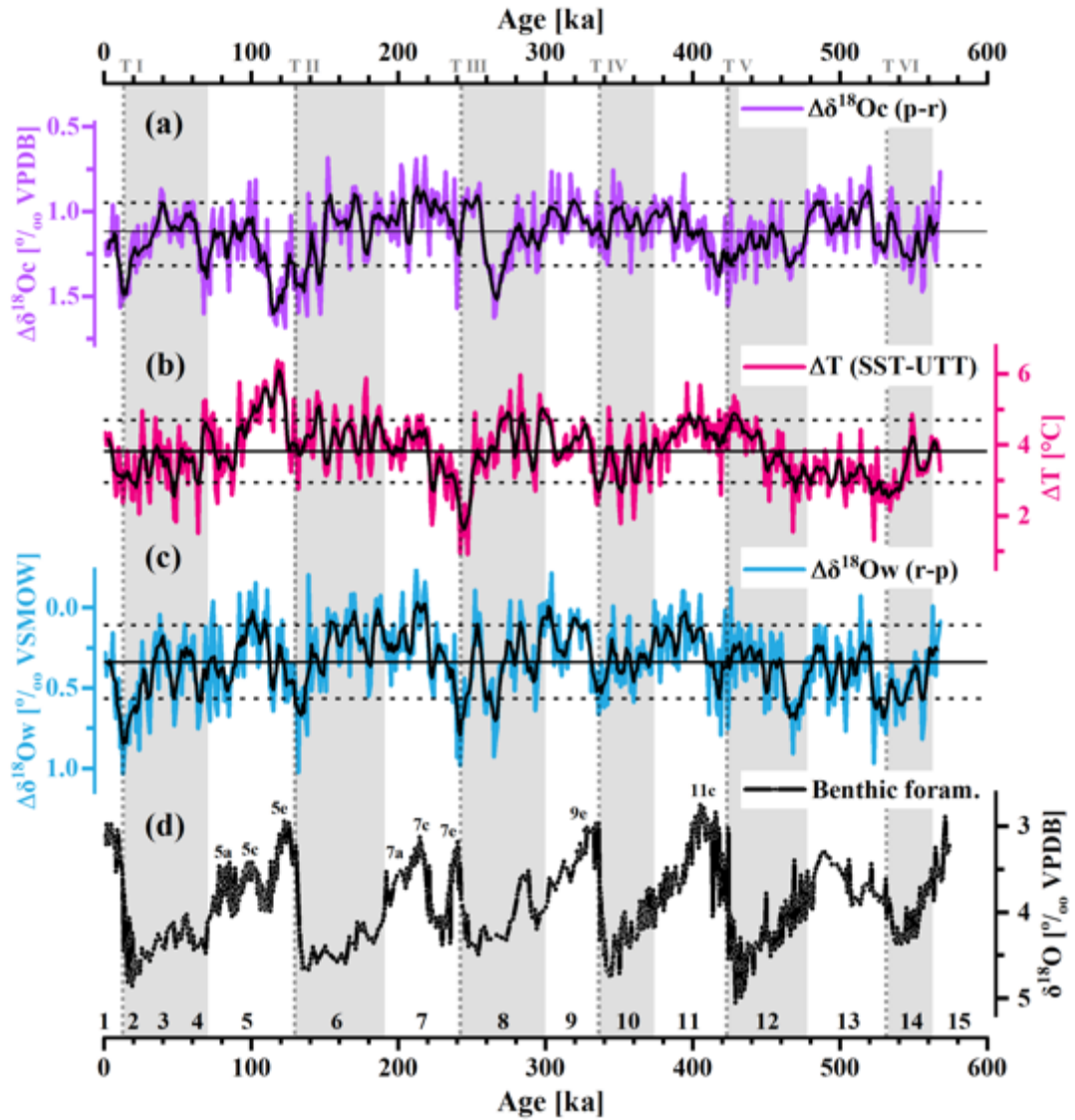
Figure 4. Solomon Sea vertical water column profile variations during the past 568-kyr. Gradients of (a) foraminiferal carbonate δ18O (Δδ18O_C), (b) inferred temperature (ΔT), and (c) inferred seawater oxygen isotope (Δδ18O_W) between *G. ruber* and *P. obliquiloculata*. Color curves represent the original data, and black curves are for the 5-point running mean. The horizontal solid and dashed black lines represent the 568-kyr average of the 5-point running mean and 1-σ range. (d) MD05-2925 benthic foraminiferal δ18O. Gray bars and dotted gray lines are glacial periods and major glacial terminations, respectively. Marine isotope stage (MIS) and substages are listed according to Lisiecki and Raymo (2005) and Railsback et al. (2015).
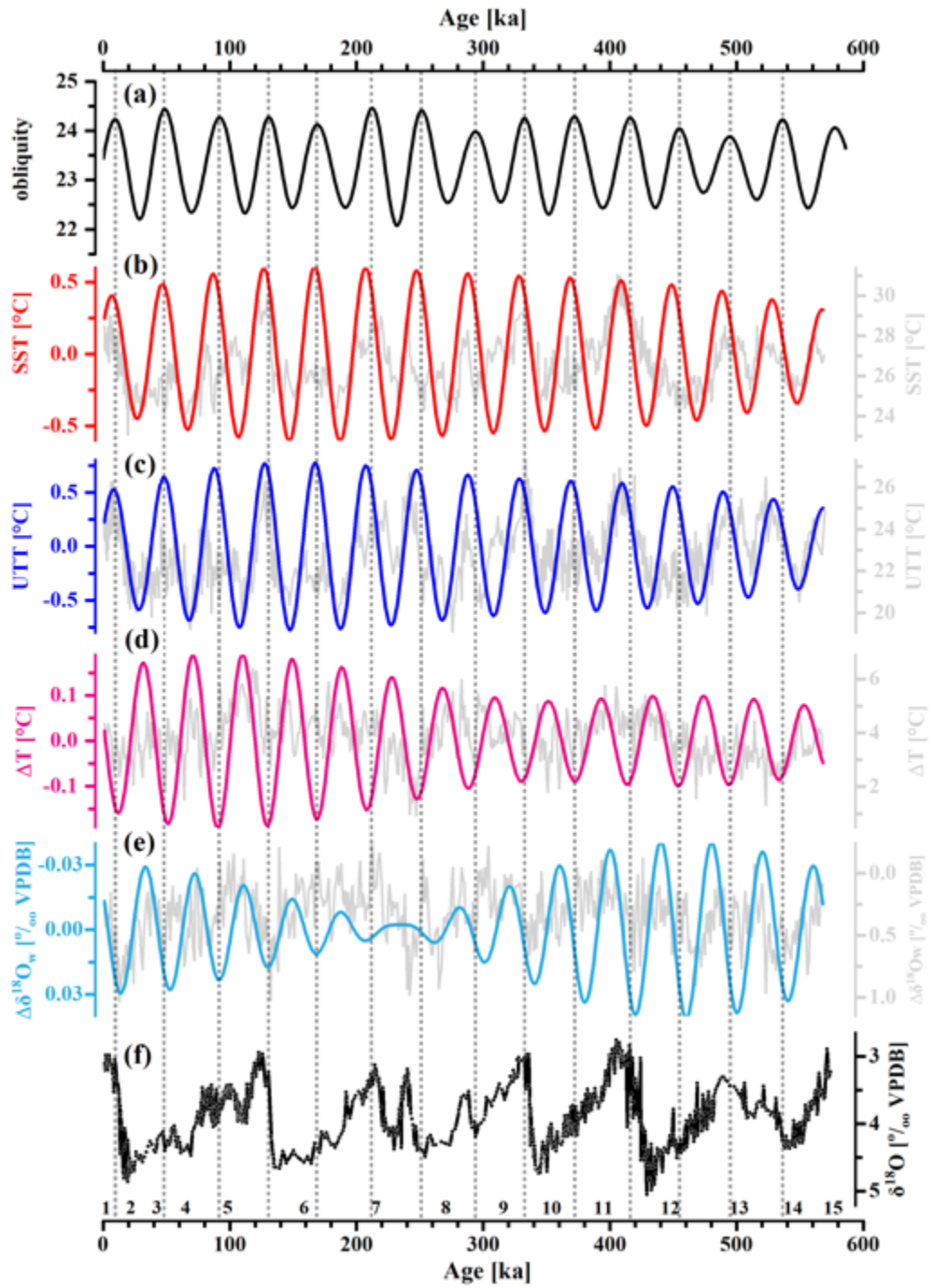
Figure 5. Obliquity band filtering of MD05-2925 geochemical results. (a) obliquity (Laskar et al., 2004), (b) SST, (c) UTT, (d) ΔT and (e) $\Delta\delta^{18}O_{w-ivc}$ and (e) MD05-2925 benthic foraminiferal $\delta^{18}O$. The black dashed lines are the synchrony line of high obliquity periods.
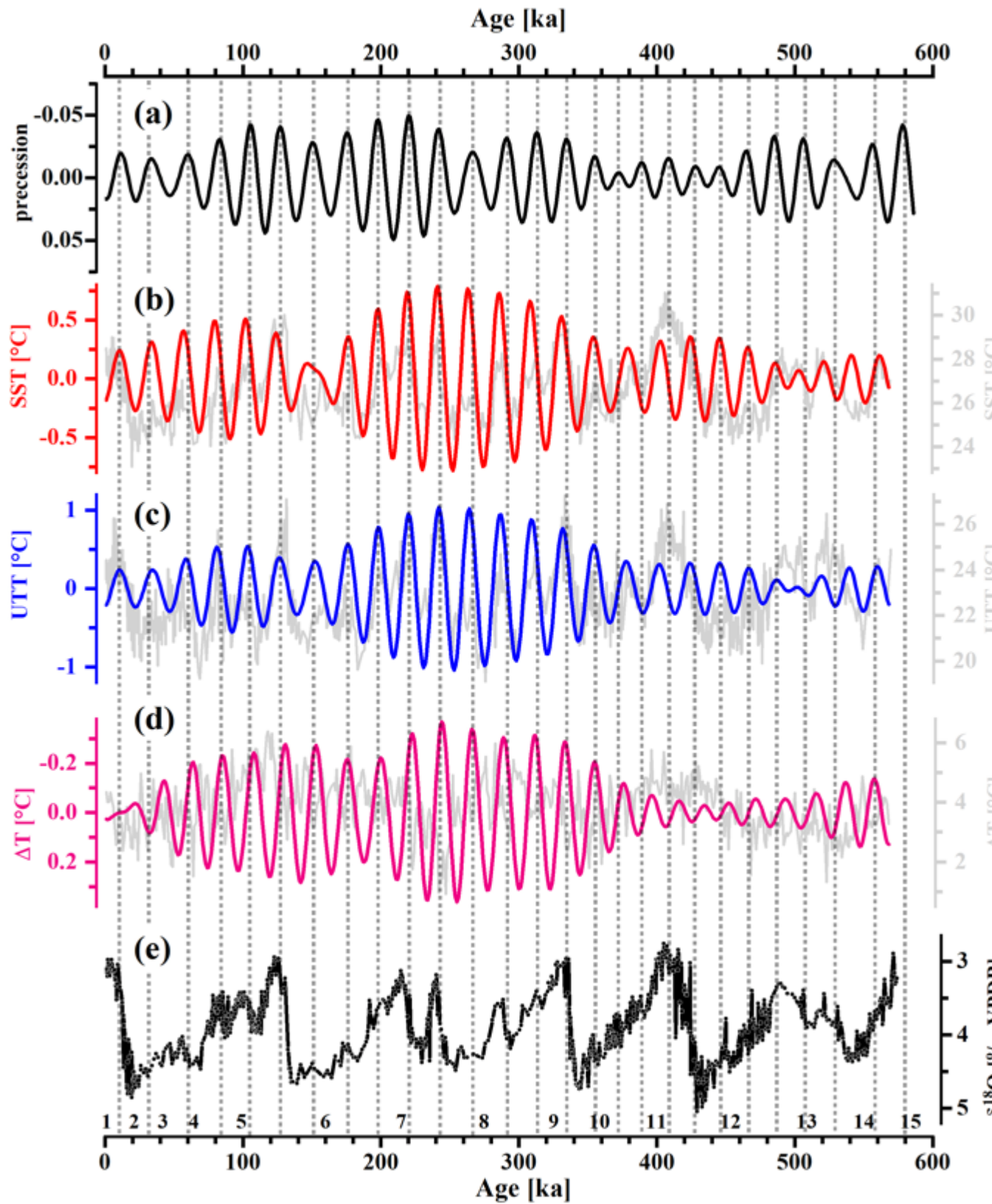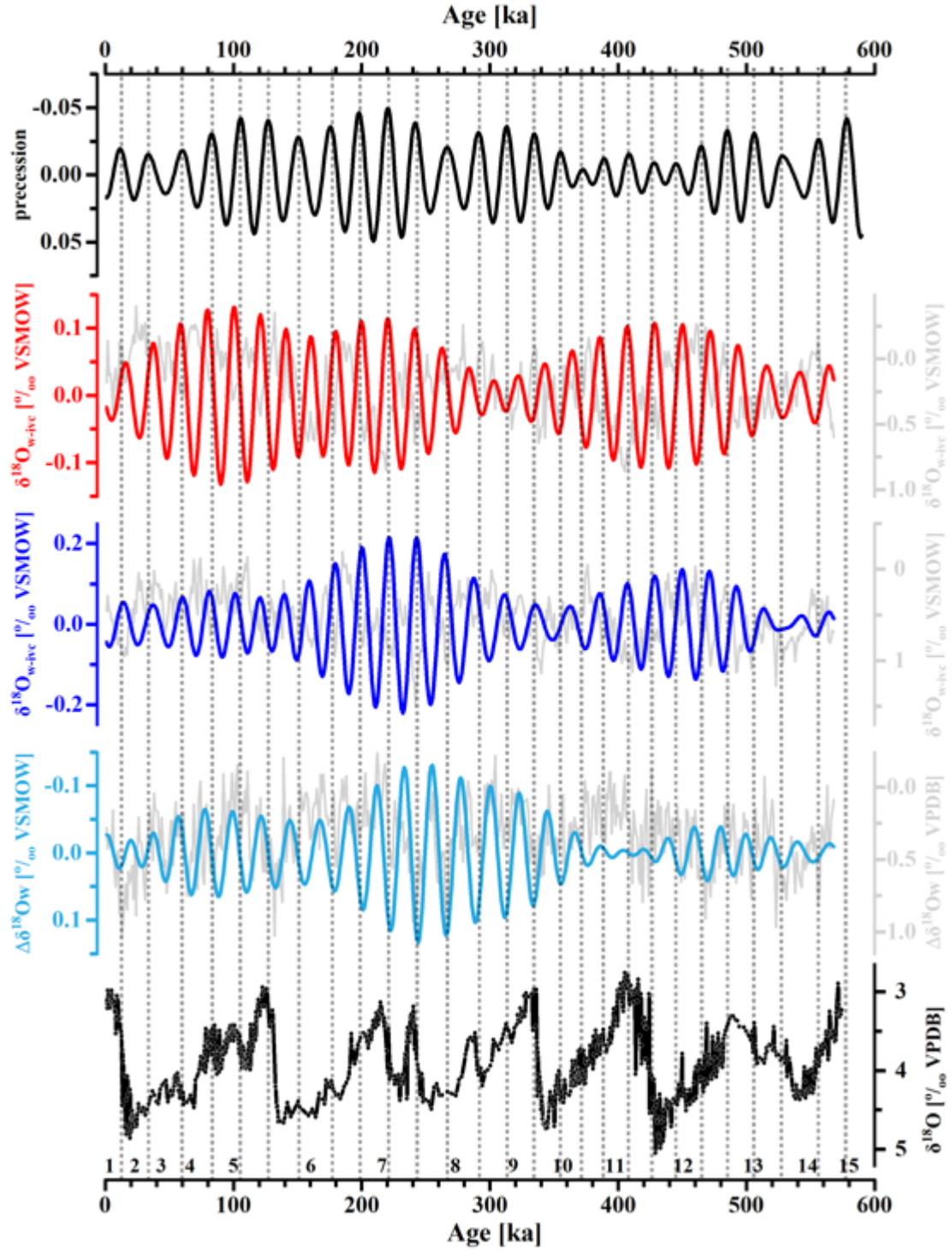
Figure 6. Precession band filtering of MD05-2925 geochemical results. (a) precession (Laskar et al., 2004), (b) SST, (c) UTT, (d) ΔT and (e) MD05-2925 benthic foraminiferal $\delta^{18}O$. The black dashed lines are the synchrony line of low precession periods.
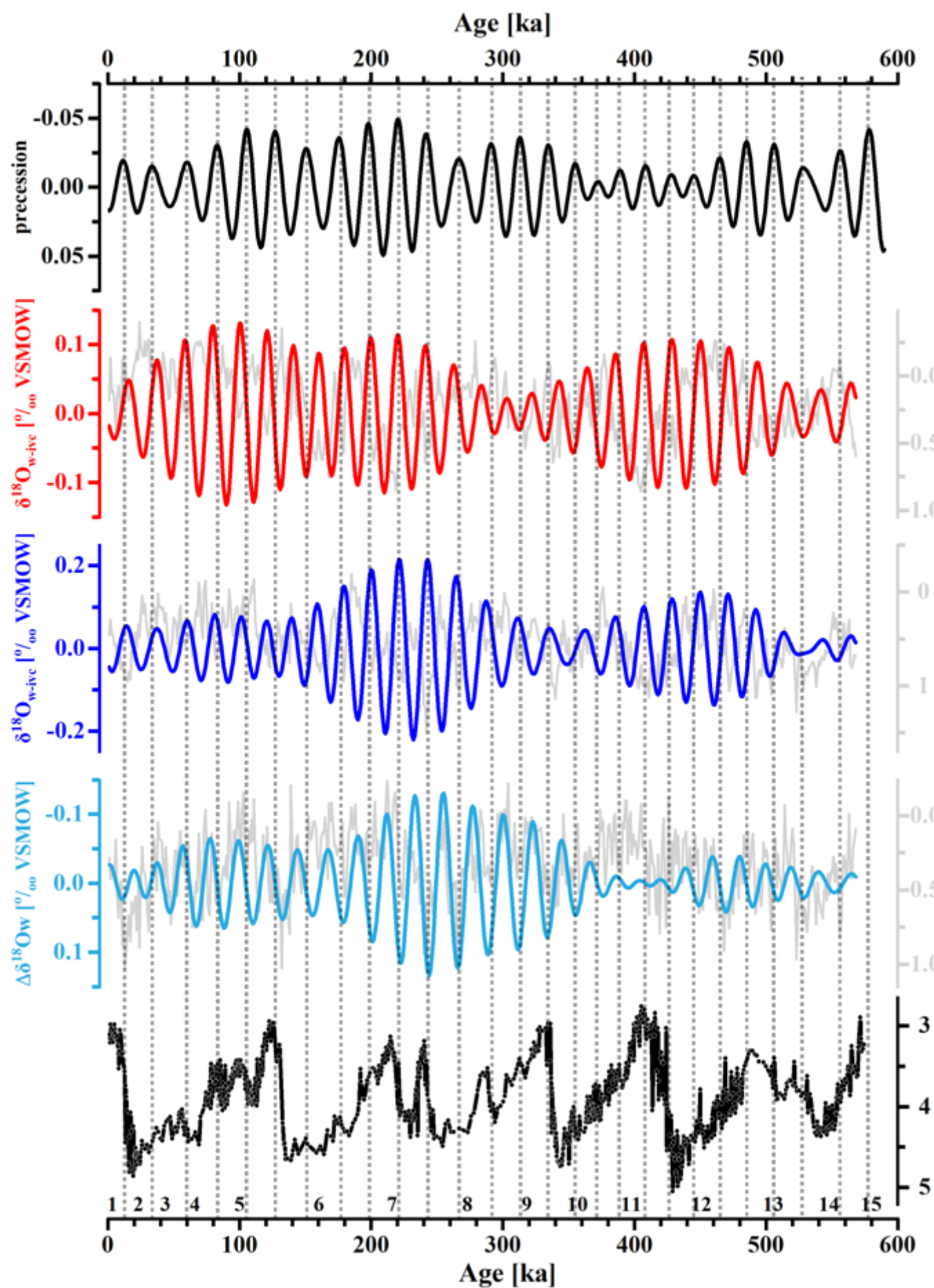
Figure 7. Precession band filtering of MD05-2925 geochemical results. (a) precession (Laskar et al., 2004), (b) surface $\delta^{18}O_{w\text{-ivc}}$, (c) subsurface $\delta^{18}O_{w\text{-ivc}}$, (d) $\Delta\delta^{18}O_{w\text{-ivc}}$ and (e) MD05-2925 benthic foraminiferal $\delta^{18}O$. The black dashed lines are the synchrony line of low precession periods.
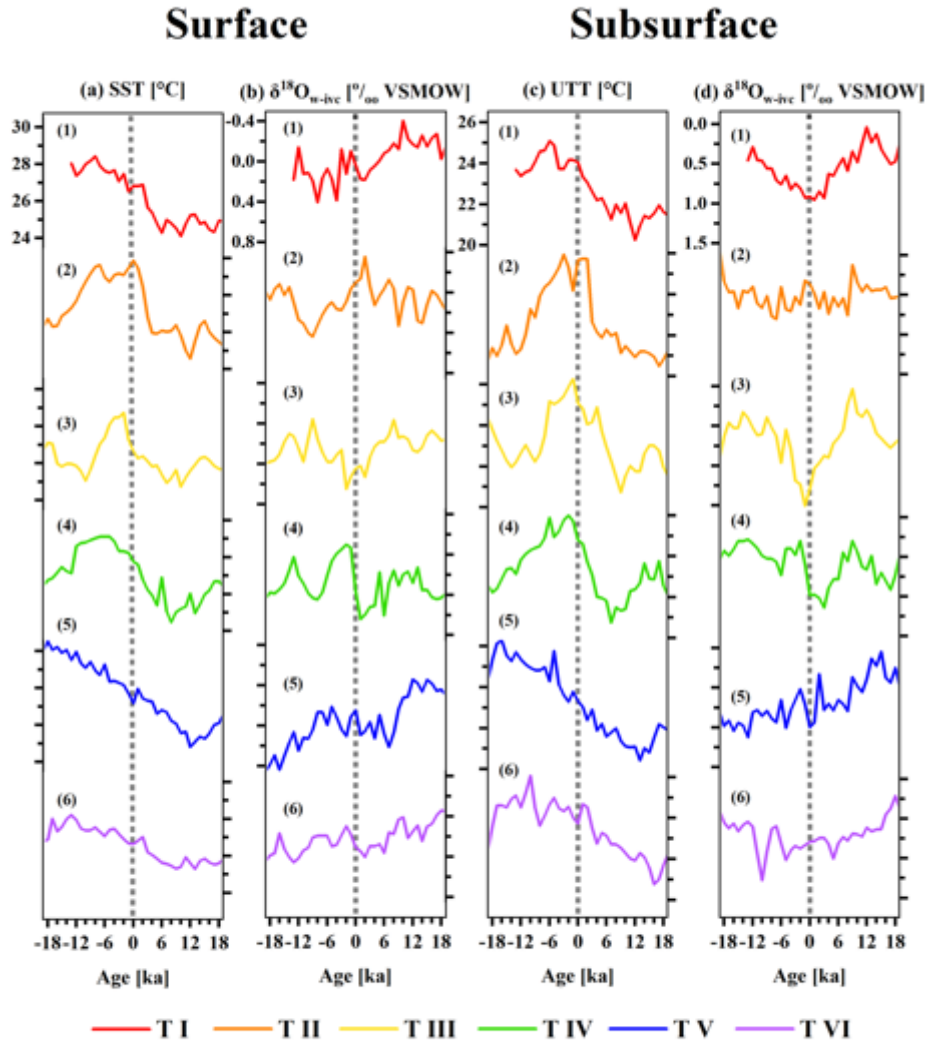
Figure 8. Comparisons of surface and upper thermocline temperature and hydrological changes of the past six terminations. (a) Sea surface temperature (SST). (b) Upper thermocline temperature (UTT). Ice-volume-corrected $\delta^{18}O$ ($\delta^{18}O_{w\text{-}ivc}$) of (c) surface and (d) subsurface waters. Dark gray line shows the Marine Isotope Stage (MIS) boundary according to Lisiecki and Raymo (2005).
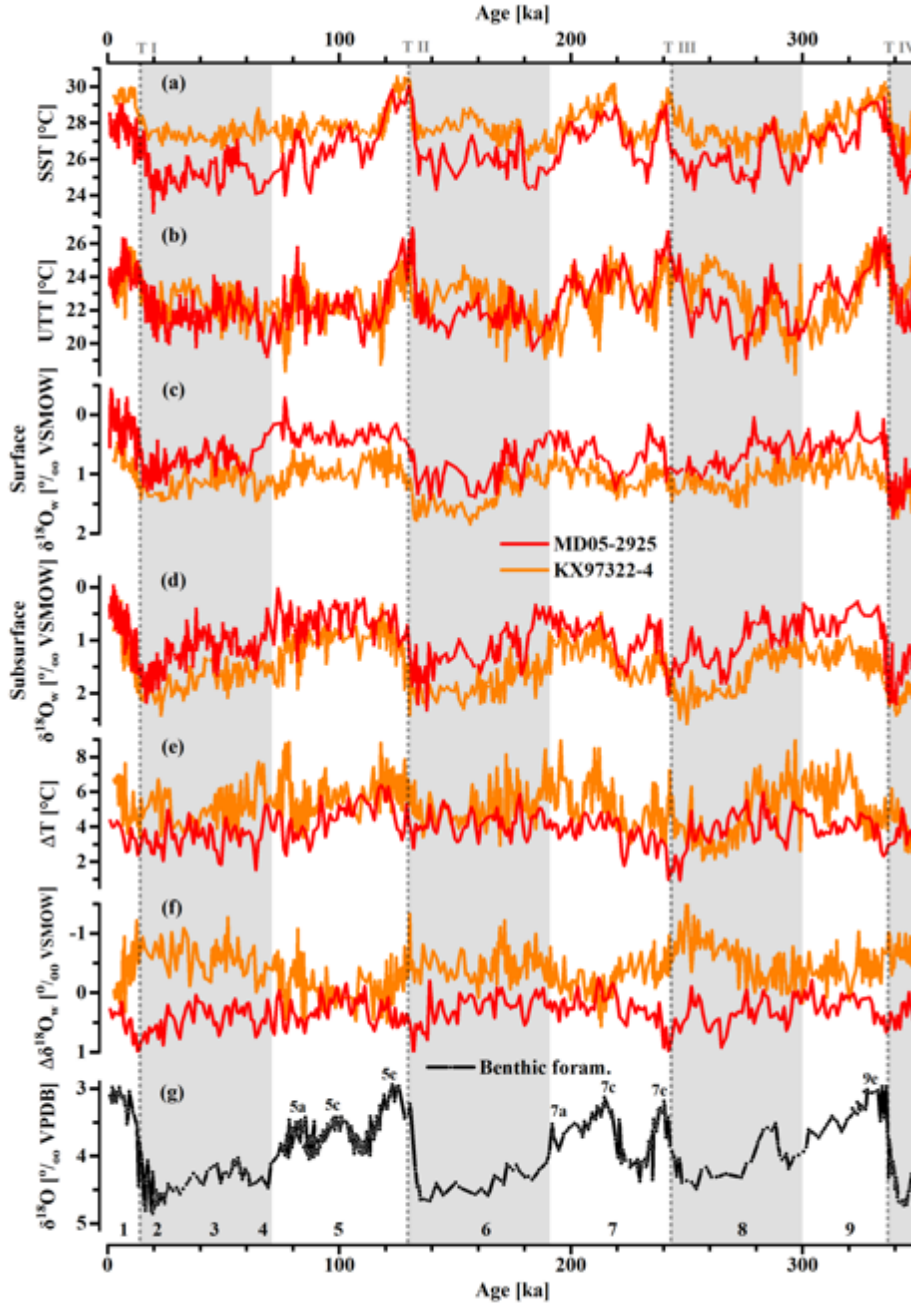
Figure 9. Regional comparison of the geochemical records between two sites in the southwest (MD05-2925, red line, this study) and central equatorial (KX97322-4, orange line, Zhang et al., 2021) Pacific. (**a**) SST, (**b**) UTT, (**c**) surface, (**d**) subsurface $\delta^{18}O_{w-ivc}$, (**e**) thermal, (**f**) hydrological gradients and (**g**) MD05-2925 benthic foraminiferal $\delta^{18}O$. Gray bars and dotted gray lines are glacial periods and major glacial terminations, respectively. Marine isotope stage (MIS) and substages are listed according to Lisiecki and Raymo (2005) and Railsback et al. (2015).

# Table

Table 1. Phase relationships.[a].

		Eccentricity (E)		Obliquity (O)		Precession (P)	
$\delta^{18}OC$	Surface	7.7 ± 17.5	7.7 ± 17.5	60.0 ± 10.8	60.0 ± 10.8	−114.5 ± 16.7	−120.1 ± 34.9
	Subsurface	10.9 ± 15.6	10.9 ± 15.6	59.4 ± 9.2	59.4 ± 9.2	−108.3 ± 19.8	−105.7 ± 29.5
	$\Delta\delta^{18}OC$	–	46.4 ± 49.1	–	54.4 ± 32.2	–	−70.0 ± 39.9
Temp.	Surface	−26.4 ± 17.8	−28.7 ± 20.4	39.8 ± 8.4	39.8 ± 8.4	−146.7 ± 18.7	−146.0 ± 25.5
	Subsurface	−44.4 ± 15.3	−44.4 ± 15.3	33.5 ± 9.3	33.5 ± 9.3	−163.2 ± 20.5	−164.3 ± 25.3
	ΔT	–	58.1 ± 33.5	−171.8 ± 23.2	−171.8 ± 23.2	−23.5 ± 13.8	−41.7 ± 37.7
$\delta^{18}OW$	Surface[b]	149.7 ± 24.1	145.9 ± 29.5	–	−120.3 ± 34.8	–	72.8 ± 53.7
	Subsurface[b]	98.1 ± 16.7	98.1 ± 16.7	–	−169.0 ± 39.1	−13.9 ± 26.4	−36.0 ± 39.3
	$\Delta\delta^{18}OW$	50.1 ± 17.2	50.1 ± 17.2	124.9 ± 27.1	124.7 ± 29.1	−56.9 ± 19.1	−58.1 ± 24.6

a

The columns in gray represent averaged phase angles that over 80% confidence level and the column in white denote the averaged phase angles of periodicities in main orbital cycles.

b

Surface and subsurface results are based on ice volume corrected seawater oxygen isotope.
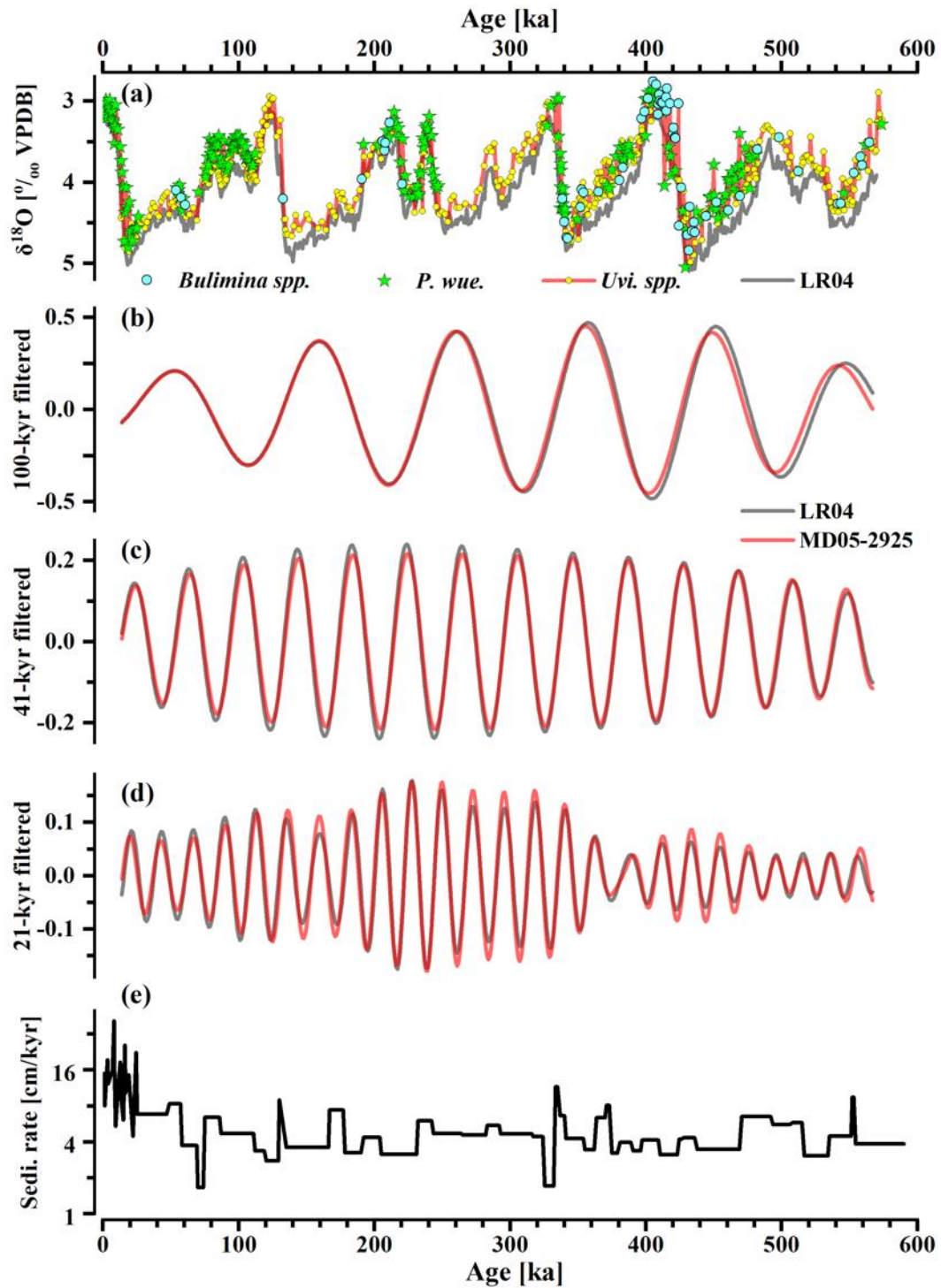
Supplementary figure 1. (a) MD05-2925 composite benthic foraminifera with different species; oxygen isotope stratigraphy with global stack LR04 (Lisiecki and Raymo, 2005). Filtering results of MD05-2925 composite benthic foraminiferal oxygen isotope stratigraphy (red lines) and LR04 (gray lines) on eccentricity (b), obliquity (c), and precession (d) bands, respectively. (e) MD05-2925 sedimentation rate log scale.
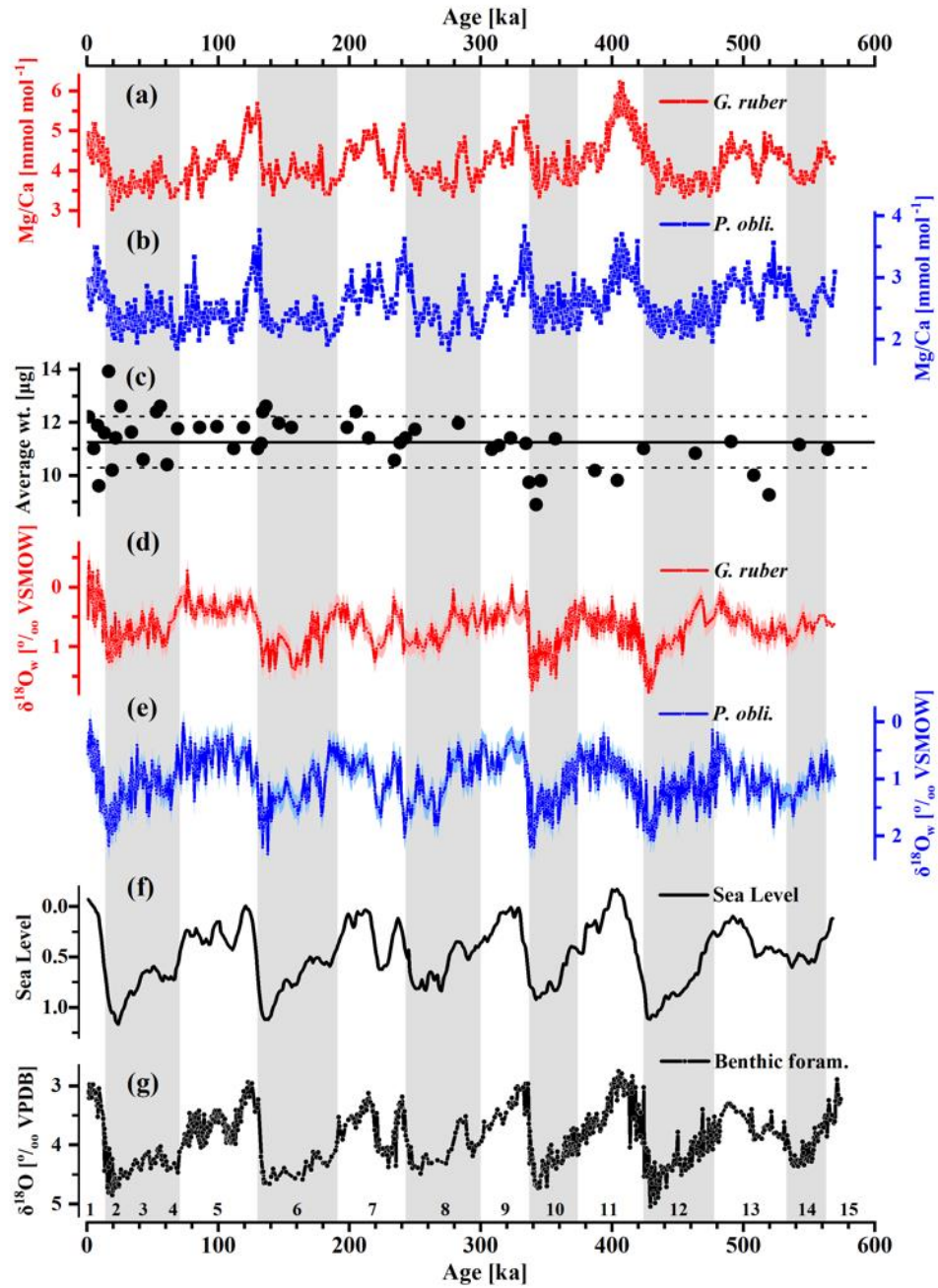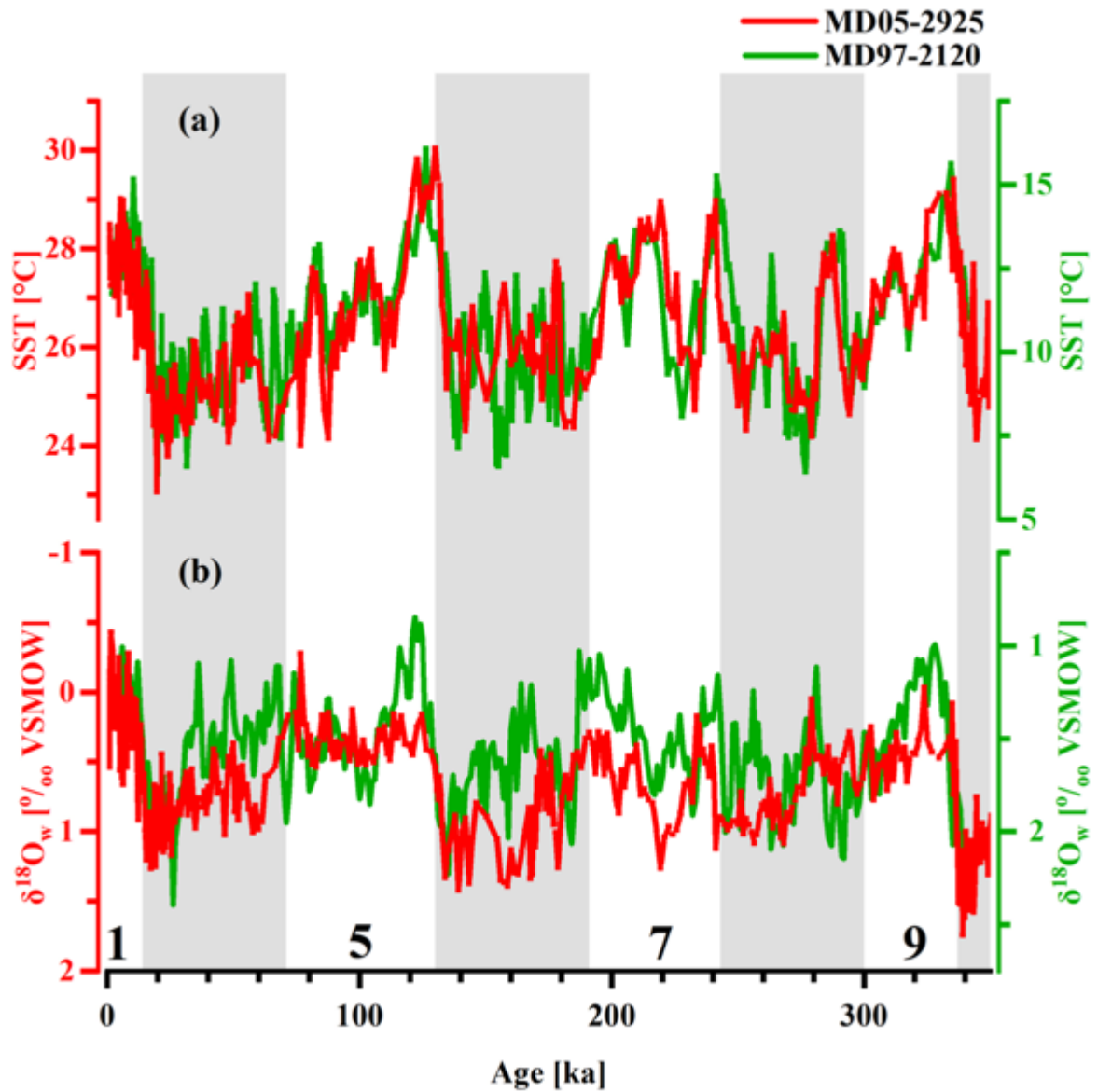
Supplementary figure 2. Records of MD05-2925 (a) surface and (b) subsurface planktonic foraminiferal Mg/Ca ratios, (c) averaged single *G. ruber* shell weight over the past 568 kyr. Inferred (d) *G. ruber* and (e) *P. obliquiloculata* seawater oxygen isotope ($\delta^{18}O_w$) time series. (f) Composite sea level (Spratt and Lisiecki, 2016). (g) MD05-2925 benthic foraminiferal $\delta^{18}O$. Gray bars denote glacial periods. Marine isotope stages (MISs) are listed according to Lisiecki and Raymo (2005). Envelopes color shading in d. and e indicate 1σ error followed Mohtadi et al. (2014) method.
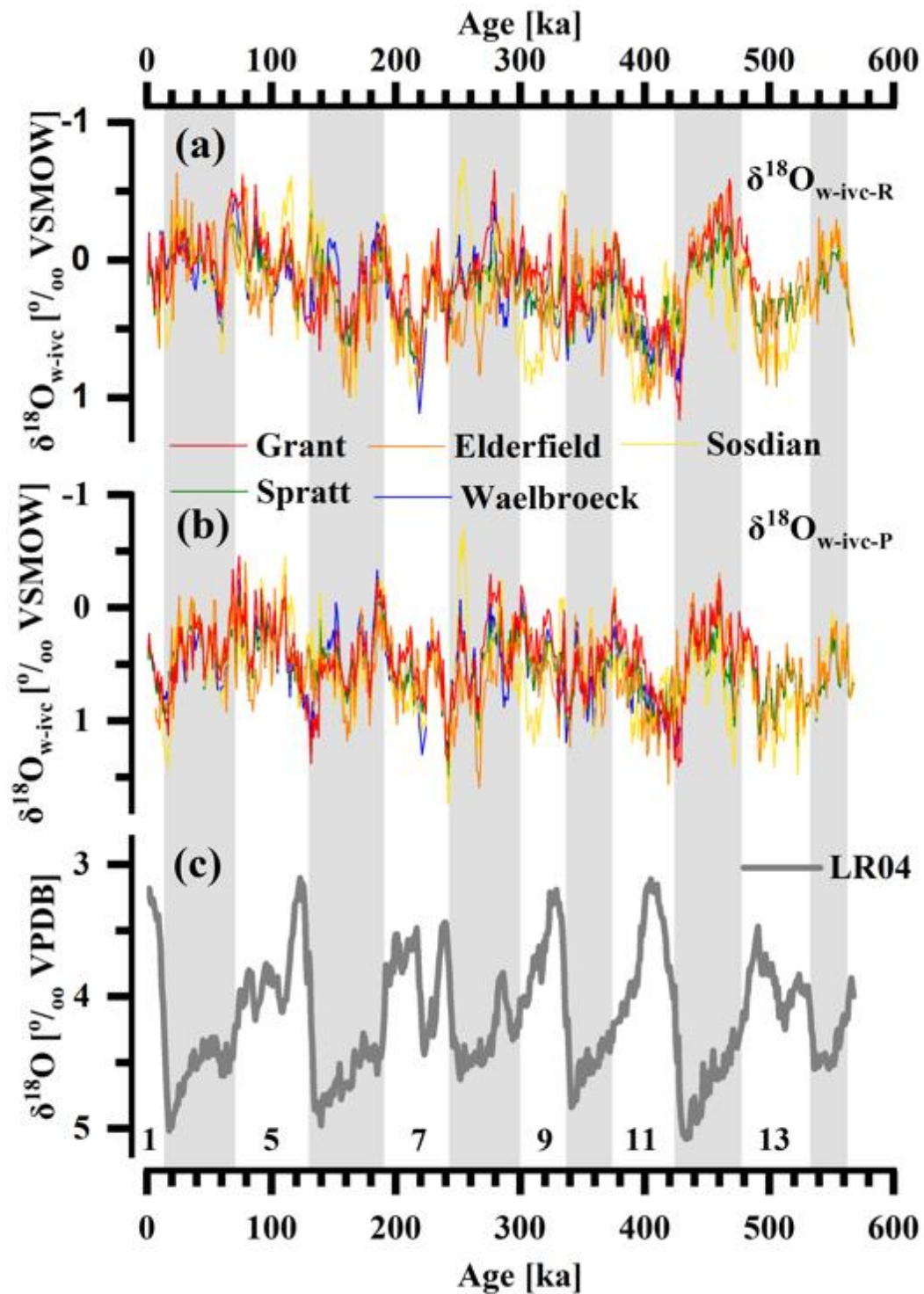
Supplementary figure 3. Comparison between ice-volume corrected seawater $\delta^{18}O$ ($\delta^{18}O_{w-ivc}$) records of (a) surface and (b) subsurface with different sea level correction models (Spratt and Lisiecki, 2016; Waelbroeck et al., 2002; Elderfield et al., 2012; Sosdian and Rosenthal, 2009) and (c) LR04 stack (Lisiecki and Raymo, 2005). Gray bars are glacial periods. Marine isotope stages (MISs) are listed according to Lisiecki and Raymo (2005).

Supplementary figure 4. Comparison of (a) SST and (b) seawater $\delta^{18}O$ ($\delta^{18}O_w$) records between MD05-2925 (red) and MD97-2120 (green, Pahnke et al., 2003). Gray bars are glacial periods. Marine isotope stages (MIS) are listed according to Lisiecki and Raymo (2005).
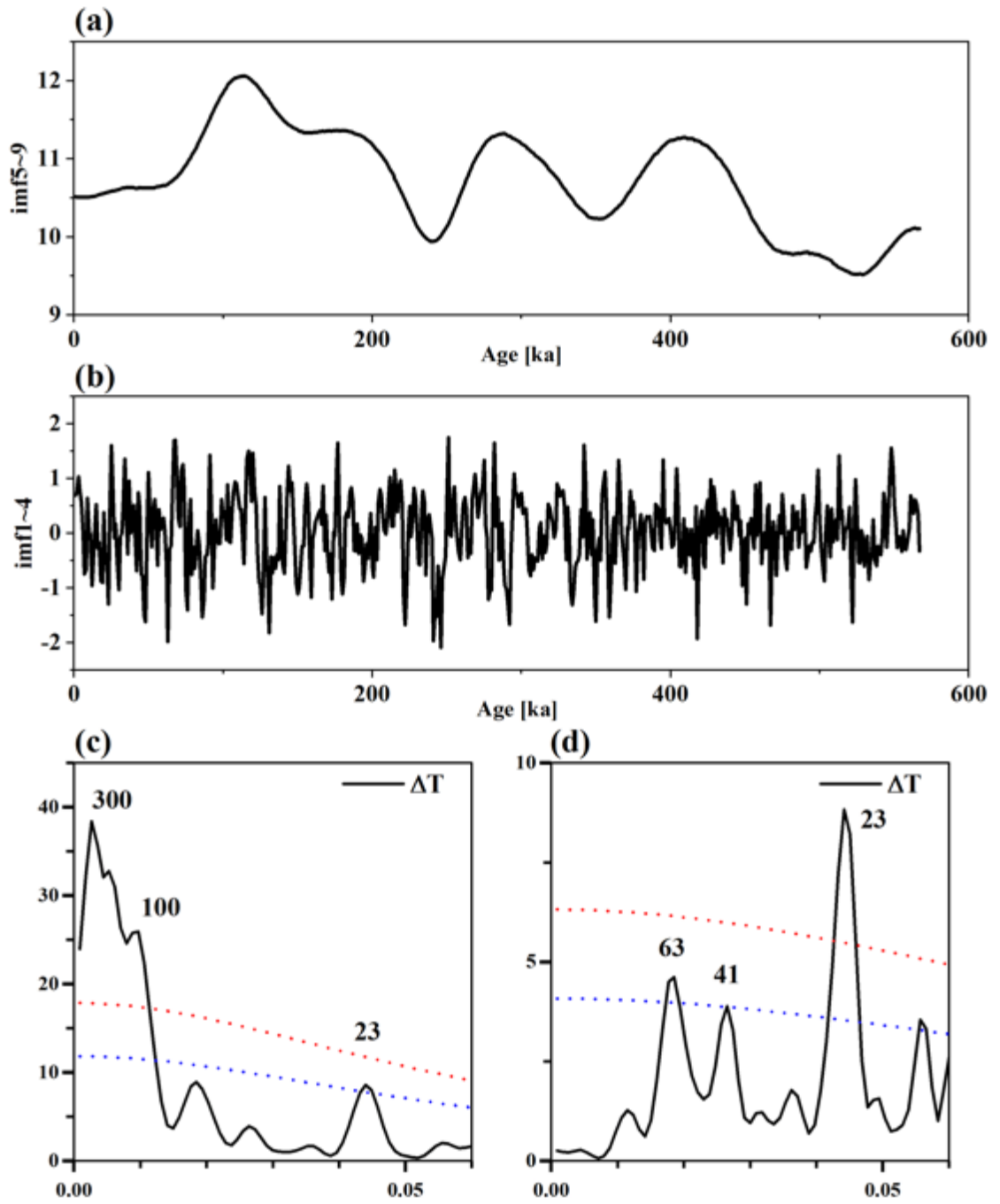
Supplementary figure 5. Ensemble Empirical Mode Decomposition (EEMD, Huang et al., 1998) results of ΔT. Composites of (a) imf 5-9 (a) and (b) imf 1-4 of MD05-2925 ΔT. Single spectrum results of (c) original ΔT and (d) imf 1-4.
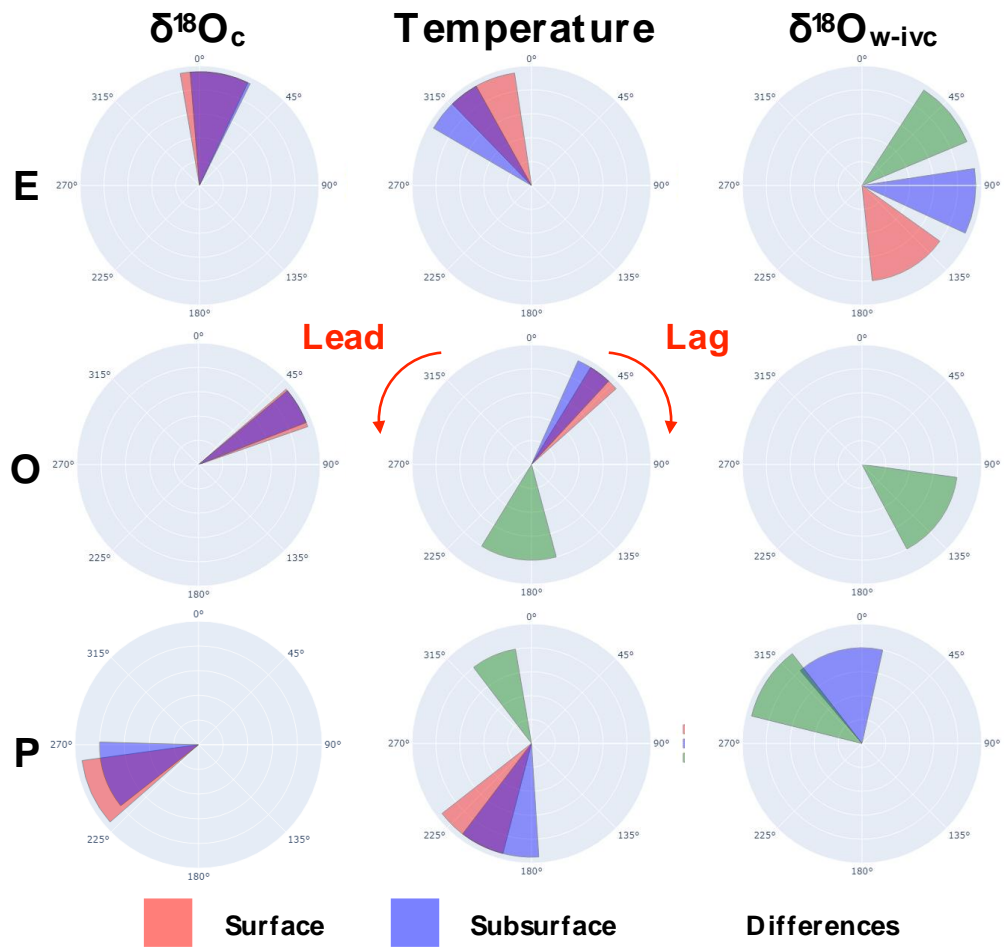
Supplementary figure 6. Phase wheel plots from the results of cross-spectral analyses between surface, subsurface, and differences of calcite $\delta^{18}O$ ($\delta^{18}O_c$), temperature, and ice-volume corrected seawater $\delta^{18}O$ ($\delta^{18}O_{w-ivc}$) records with eccentricity (E), obliquity (O), and precession parameters (P), respectively (Laskar et al., 2004).

References

Elderfield, H., Ferretti, P., Greaves, M., Crowhurst, S., McCave, I.N., Hodell, D., Piotrowski, A.M., 2012. Evolution of ocean temperature and ice volume through the Mid-Pleistocene climate transition. Science 337, 704-709

Huang, N.E., Shen, Z., Long, S.R., Wu, M.C., Shih, H.H., Zheng, Q., Yen, N.-C., Tung, C.C., Liu, H.H., 1998. The empirical mode decomposition and the Hilbert spectrum for nonlinear and non-stationary time series analysis. Proceedings of the Royal Society A: Mathematical, Physical and Engineering Sciences 454, 903-995.

Laskar, J., Robutel, P., Joutel, F., Gastineau, M., Correia, A., Levrard, B., 2004. A long-term numerical solution for the insolation quantities of the Earth. Astronomy & Astrophysics 428, 261-285. https://doi.org/10.1051/0004-6361:20041335.

Lisiecki, L.E., Raymo, M.E., 2005. A Pliocene-Pleistocene stack of 57 globally distributed benthic $\delta^{18}O$ records. Paleoceanography 20. https://doi.org/10.1029/2004PA001071.

Mohtadi, M., Prange, M., Oppo, D.W., De Pol-Holz, R., Merkel, U., Zhang, X., Steinke, S., Lückge, A., 2014. North Atlantic forcing of tropical Indian Ocean climate. Nature 509, 76-80.

Pahnke, K., Zahn, R., Elderfield, H., Schulz, M., 2003. 340,000-year centennial-scale marine record of southern hemisphere climatic oscillation. Science 301, 948-952.

Sosdian, S., Rosenthal, Y., 2009. Deep-sea temperatura and ice volumen changes across the Pliocene-Pleistocene climate transitions. Science 325, 306-310.

Spratt, R.M., Lisiecki, L.E., 2016. A Late Pleistocene sea level stack. Climate of the Past 12, 1079-1092. https://doi.org/10.5194/cp-12-1079-2016.

Waelbroeck, C., Labeyrie, L., Michel, E., Duplessy, J.C., McManus, J.F., Lambeck, K., Balbon, E., Labracherie, M., 2002. Sea-level and deep water temperature changes derived from benthic foraminiferal isotopic records. Quaternary Science Reviews 21, 295-305.